Properties of Arctic aerosol in the transition between Arctic haze to summer season derived by lidar

Nele Eggers

Contents

List of Figures

List of Tables

Selbstständigkeitserklärung

Hiermit erkläre ich, dass ich diese Arbeit selbständig verfasst und keine anderen als die von mir angegebenen Hilfsmittel genutzt habe. Sämtliche Stellen der Arbeit, in denen Inhalt aus diesen Quellen wörtlich oder inhaltlich entnommen wurde, sind als solche kenntlich gemacht. Diese Arbeit hat in gleicher oder ähnlicher Form noch keiner Prüfungsbehörde vorgelegen und wurde nicht veröffentlicht.

Potsdam, 09.08.2023   Nele Eggers

Properties of Arctic aerosol in the transition between Arctic haze to summer season derived by lidar

Nele Eggers

Abstract

During the Arctic haze period, the Arctic troposphere consists of larger, yet fewer, aerosol particles than during the summer (Tunved et al., 2013; Quinn et al., 2007). Interannual variability (Graßl and Ritter, 2019; Rinke et al., 2004), as well as unknown origins (Stock et al., 2014) and properties of aerosol complicate modeling these annual aerosol cycles. This thesis investigates the modification of the microphysical properties of Arctic aerosols in the transition from Arctic haze to the summer season. Therefore, lidar measurements of Ny-Ålesund from April 2021 to the end of July 2021 are evaluated based on the aerosols' optical properties. An overview of those properties will be provided. Furthermore, parallel radiosonde data is considered for indication of hygroscopic growth.

The annual aerosol cycle in 2021 differs from expectations based on previous studies from Tunved et al. (2013) and Quinn et al. (2007). Developments of backscatter, extinction, aerosol depolarisation, lidar ratio and color ratio show a return of the Arctic haze in May. The haze had already reduced in April, but regrew afterwards.

The average Arctic aerosol displays hygroscopic behaviour, meaning growth due to water uptake. To determine such a behaviour is generally laborious because various meteorological circumstances need to be considered. Two case studies provide further information on these possible events. In particular, a day with a rare ice cloud and with highly variable water cloud layers is observed.

Properties of Arctic aerosol in the transition between Arctic haze to summer season derived by lidar

Nele Eggers

Zusammenfassung

Während der *Arctic haze* Periode sind größere, jedoch auch weniger, Aerosole in der arktischen Troposphäre vorhanden als im Sommer (Tunved et al., 2013; Quinn et al., 2007). Interannuale Variabilität (Graßl and Ritter, 2019; Rinke et al., 2004), sowie unbekannte Herkunft (Stock et al., 2014) und Eigenschaften der Aerosole erschweren die Modellierung der Aerosol-Jahresgänge. Diese Arbeit untersucht, wie sich die mikrophysikalischen Eigenschaften der Aerosole beim Übergang vom *Arctic haze* zur Sommerzeit ändern. Dafür werden Lidar Messungen aus Ny-Ålesund von April 2021 bis Ende Juli 2021 hinsichtlich der optischen Eigenschaften der Aerosole untersucht. Ein Überblick über diese Eigenschaften wird gegeben. Zusätzlich werden parallele Radiosondendaten mit einbezogen, um Hinweise auf hygroskopisches Wachstum zu erhalten.

Der Jahresgang der Aerosole in 2021 unterscheidet sich von Erwartungen, gebildet aus früheren Studien von Tunved et al. (2013) und Quinn et al. (2007). Die zeitliche Entwicklung des Rückstreuungskoeffizienten, Extinktionskoeffizienten, der Aerosol Depolarisation, des Lidarverhältnisses und des Farbverhältnisses zeigen, dass der Arctic haze im Mai zurückkehrt. Im April hatte der haze bereits abgenommen, stieg in Mai jedoch wieder an.

In der Arktis zeigt ein Aerosol typischerweise hygroskopisches Verhalten - mit anderen Worten, es wächst durch Aufnahme von Wasser. Ein solches alleine aus Fernerkundungsdaten zu bestimmen ist jedoch in der Regel aufwendig, weil unterschiedliche meteorologische Bedingungen zu berücksichtigen sind. Zwei Fallstudien geben mehr Informationen über die möglichen hygroskopischen Verhaltensweisen der Aerosole. Insbesondere wird auch ein Tag mit einer Eiswolke und stark fluktuierenden Wasserwolken beobachtet.

1. Introduction

The Arctic is a key region in understanding Earth's climate system. Due to *Arctic Amplification*, Arctic regions experience enhanced warming. This amounts to a factor of two to four in future predictions (IPCC, 2021). Despite knowledge gained since the last IPCC report in 2013 (IPCC, 2021), the prediction of Arctic Amplification is imprecise and complex, due to the interaction between a variety of processes (IPCC, 2021; Schmale et al., 2021). In particular, aerosol impacts and aerosol-cloud interactions are poorly represented by models. However, these effects have a key impact on the Arctic radiative budget. They thus lead to great uncertainties in climate predictions (Li et al., 2022; IPCC, 2021; Schmale et al., 2021; Tunved et al., 2013)

Modeling of aerosols is a complex topic, due to the dependence of aerosol properties on many factors, like origin, size and chemical reactivity. Different aerosol species are present in the Arctic troposphere. Reasons for such differences are, for instance, the transport of aerosols into the Arctic, and the variety of aerosol sources (Stohl, 2006; Quinn et al., 2007; Boucher, 2015). Hence, aerosol occurrence differs depending on location (Rinke et al., 2004) and season (Tunved et al., 2013), and thus the aerosols' radiative impact (Nakoudi et al., 2020).
In particular, the aerosols might change their physical properties in humid regions due to water uptake. This phenomenon is called *hygroscopic growth* (Vu et al., 2021; Zieger et al., 2013).

In order to increase the accuracy of the climate models, further knowledge about the temporal and spatial development of the aerosols' microphysical properties is necessary (Tunved et al., 2013). Measurements of those are obtained by in-situ and remote sensing devices, like lidar. A lidar provides vertically resolved profiles of the optical aerosol properties. The microphysical properties may then be obtained by inversion of the scattering problem.
There are several studies on annual aerosol cycles and hygroscopic growth. In-situ measurements show that fewer, but larger, aerosols are present in Arctic spring, while the aerosol accumulation of early summer consists of a higher number density, but a smaller diameter (Tunved et al., 2013). Remote sensing devices display a weaker transition of those seasonal-dependent properties, due to integration of the air column above.

The entirety of aerosol processes is difficult to model despite the present variety of studies (Li et al., 2022). To give an illustration of complications: Interannual variability, special meteorological events (like ice clouds), as well as alteration of the aerosols' radiative effect, which depends on external circumstances, cause the modeling of aerosols to be highly complex.

Therefore, amongst other things, aforesaid external circumstances, like sun position, height, and surface albedo, must be considered. In addition, complications in determining physical properties of the aerosols via in-situ or remote sensing devices can occur. Because of temporal and spatial shifts of these two measurements they might record two different effects, i.e. for short-lived effects. Further research is necessary to treat a variety of aerosol behaviours that are not yet covered by models. A summarizing simplification towards a model of a *general Arctic aerosol effect* is desirable.

The aim of this thesis is to investigate the physical properties of Arctic aerosols from April 2021 to the end of July 2021, using lidar. Parallel radiosonde data provide indications of hygroscopic growth.

2. Theoretical background

A scientific knowledge basis to this thesis is introduced here. First, aerosols and clouds, i.e. their interaction and impact on the radiative budget, are summarized. An explanation and a mathematical description of the *hygroscopic growth* phenomenon of aerosols follows. In subsection 2.2 the Arctic year is divided into three parts, according to the annual Arctic aerosol patterns. General scattering properties of aerosols and air molecules, as well as the Mie theory, are gathered in subsection 2.3.

2.1. Aerosols and clouds

Aerosols and clouds both influence the *net radiative balance* or *radiative budget*, due to interaction with radiation from space and/or Earth. This budget is defined through the relation of solar radiation approaching the Earth and radiation sent from Earth back to space (NASA earth observatory, 1999). Moreover, the radiation budget is a key component to defining the state of the Arctic climate.

On global average, clouds' radiative impacts lead to a cooling of the Earth's surface. The Polar regions are special, where the presence of aerosols and clouds leads to a warming effect (Schmale et al., 2021; Hartmann et al., 1992). Further explanations follow in subsection 2.1.1.

Cloud occurrence depends on aerosols, as cloud droplets nucleate at specific kinds of aerosols. These aerosols are called *cloud condensating nuclei* (CCN) (Schmale et al., 2021; IPCC, 2021) and *ice nucleating particles* (INP) (Curry et al., 1996). The following section provides deeper knowledge regarding effects of aerosols and clouds on the climate system, and the aerosol-cloud interactions.

2.1.1. The radiative effect of aerosols and clouds in the climate system

Aerosols are small particles in the atmosphere. The atmosphere can only be cleared of aerosols by direct *dry deposition* to the surface or *wet deposition*, hence falling to the surface due to precipitation. Aerosols typically spend a lifetime between just a few minutes up to several weeks in the troposphere (Haywood and Boucher, 2000). They stem from either anthropogenic or natural emissions. Via scattering and absorption of solar radiation, as well as cloud-interactions they affect the radiative budget. The effect of aerosols on the climate is determined by their

main properties: size, chemical composition and particle shape (Boucher, 2015). The sizes range typically from $0.001\,\mu$m to $10\,\mu$m (Haywood and Boucher, 2000). Different classifications for aerosol particles are (Boucher, 2015):

1. Primary and Secondary particles: Primary particles are directly emitted into the atmosphere, whilst secondary particles form via condensation of gases, called *aerosol precursors*.

2. Aerosol particles can also be classified by regions of appearance, due to spatial differences of aerosol populations (e.g. urban, semiurban, continental, desertic, marine, volcanic and stratospheric aerosols). However, due to the complexity of aerosol emission and transport, mixtures of aerosol species are typically observed; hence this nomenclature provides a rough overview only.

3. The last classification is by their origin: One can either define natural aerosols or anthropogenic aerosols. Aerosols through emissions from the ocean, soils, vegetation, fires and volcanos are classified as natural aerosols. Whereas, biomass burning is a great source of anthropogenic aerosols. Human-caused vegetation fires are categorised as origin of anthropogenic aerosols, too.

As stated before, aerosols impact the climate system, especially by influencing its radiative balance either directly through scattering and absorbing solar radiation (*aerosol direct effect*), or indirectly through *aerosol-cloud interactions* by determining and altering cloud properties. The indirect effect refers to the fact that, given sufficient size, aerosols can act as a *cloud condensation nuclei* (CCN) and form cloud droplets (Schmale et al., 2021; Curry et al., 1996). In addition, water-soluble aerosols can grow due to coagulation, till they operate as CCN, too (Boucher, 2015). The two main indirect effects are the *cloud albedo effect*, or *Twomey effect* after Twomey (1977), and the *cloud lifetime effect*. They affect the scattering or precipitation efficieny of the cloud, respectively. This results in an enhanced cooling effect (Lohmann and Feichter, 2005). Further explanations to these two indirect effects, and the direct aerosol effect, are gathered in figure 2.1.

By contrast to CCN, only few aerosols can act as *ice nucleating particles* (INP) and form ice clouds (Curry et al., 1996). Deeper knowledge about INP is still missing in observations, as well as simulations. Unstable INP simulations cause climate models, that include aerosol-cloud interactions, to contain large uncertainties. Future studies should focus on both, advancing the observation of INP and implementing INP into models, according to these observations (Burrows et al., 2022).

Clouds influence the radiative budget (IPCC, 2021; Rosenfeld et al., 2014). Hartmann et al. (1992) investigated how different cloud types differ in their impact on the Earth's energy bal-

Direct effect

solar radiation — Reflect — Absorb — Aerosol

Indirect effect

1) Cloud-Albedo effect

2) Cloud lifetime effect
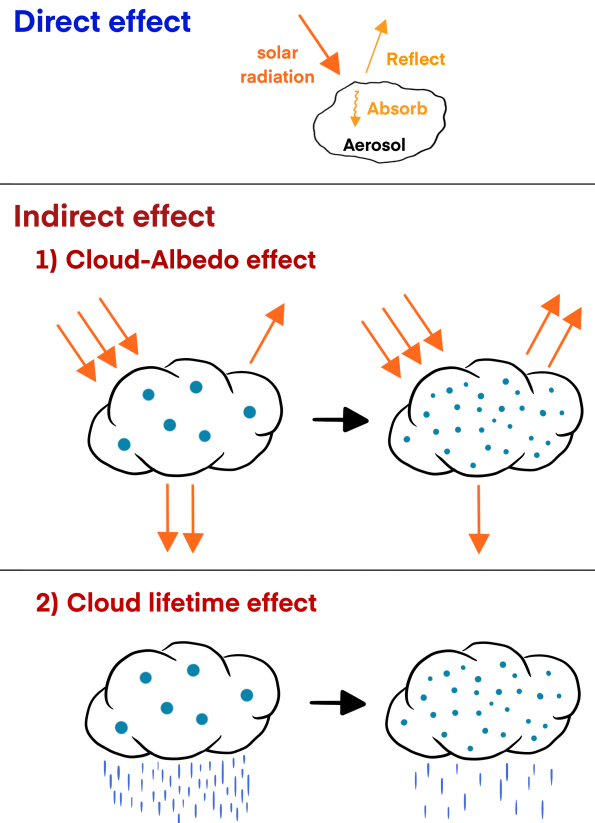
Figure 2.1.: The direct and indirect aerosol effects are illustrated. These effects are gathered in IPCC (2021). Lohmann and Feichter (2005) pursued further research to the indirect aerosol effects. Aerosols interact with the climate system directly by scattering and absorbing solar radiation. Their indirect effect is subdivided into the *cloud albedo effect*, or *Twomey effect* after Twomey (1977), and the *cloud lifetime effect*. The first indirect effect, the cloud-albedo effect, says that clouds with more, yet smaller aerosol particles, block more solar radiation. The second indirect effect states that clouds with more, yet smaller aerosols, are less efficient in precipitating, and therefore these clouds have an extended lifetime.

ance. In particular, two cloud types will be highlighted here:

Researchers mostly deal with *low-level* clouds. These optical thick clouds are cooling the climate system, due to their high *cloud albedo forcing* and low *cloud greenhouse forcing*. Cloud albedo forcing refers to the ability of clouds to reflect short-wave solar radiation back into space, whereas cloud greenhouse forcing describes the warming effect of clouds interacting with long-wave radiation of the Earth's surface. By contrast, *high-level* clouds tend to warm the Earth (Hartmann et al., 1992; Rosenfeld et al., 2014). Figure 2.2 summarizes aforesaid interaction properties of the two cloud types with radiation.

On global average, clouds cause a cooling effect. Yet, the global average cooling effect of clouds is expected to decrease as time passes. (IPCC, 2021).

High-level clouds
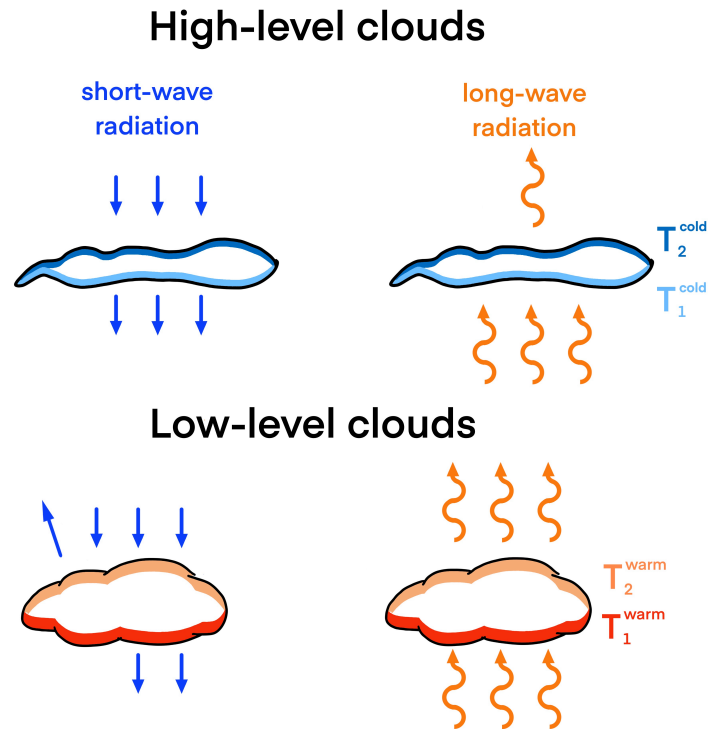
Low-level clouds

Figure 2.2.: Scheme of radiative interactions of low- and high-level clouds with short- and long-wave radiation. According to NASA earth observatory (1999), low-level clouds scatter around one third of incoming short-wave radiation back into space. Long-wave radiation from Earth's surface is almost completely transmitted by them. In contrast, high-level clouds let more short-wave radiation and less long-wave radiation through. NASA earth observatory (1999) states optical thickness and temperature to be main drivers of these effects. Thereby, for the temperatures of the clouds holds: $T_1^{\mathrm{warm}} > T_2^{\mathrm{warm}} \gg T_1^{\mathrm{cold}} > T_2^{\mathrm{cold}}$.

Aerosol and cloud phenomenons of the Arctic differ from the global average.

The overall effect of Arctic clouds is not a cooling effect like it is the case for other latitudes. The cloud greenhouse forcing of low-level clouds outbalances their albedo forcing, thus inducing a warming effect. This surface warming stems from re-emission of long-wave radiation from Earth's surface. Therefore, the effect is the strongest in seasons without sunlight, i.e. the polar night (Schmale et al., 2021).

A variety of aerosol species emerge in the Arctic atmosphere due to natural processes or transport patterns, i.e. sulphates and black carbon from biomass burning (Zielinski et al., 2020). Arctic aerosol species, and especially their seasonality and radiative impact, will be discussed further in subsection 2.2.

Effects of aerosols to the Arctic climate system can be divided into two categories (Schmale et al., 2021):

1. *Local effects* arise only through inner-Arctic processes and have the ability to influence cloud properties, radiative fluxes and the Arctic energy balance.

2. *Remote effects* are caused by changes in aerosol pollutions outside the Arctic, e.g. in the mid-latitudes and tropics. They impact the Arctic climate conditions by altering the radiation balance, thus the meridional heat transport.

2.1.2. Hygroscopicity of aerosols

Hygroscopicity of aerosols denotes their ability to grow due to uptake of water vapour. Changes in size distribution of aerosol particles modify their scattering and absorption abilities, hence the radiative balance of the climate system (Vu et al., 2021). Further knowledge about the hygroscopicity of aerosols is necessary for investigation of cloud properties. The chemical composition of aerosols determines their hygroscopic characteristics. Hence the spatial and temporal distribution in aerosols' chemical composition has to be taken into account, as stated by Swietlicki et al. (2008), mentioned by Vu et al. (2015).

A measure of the hygroscopicity is the *hygroscopic growth factor* (Vu et al., 2021; Zieger et al., 2013)

$$\text{Gf(RH)} = \frac{\text{D}_{\text{wet}}(\text{RH})}{\text{D}_{\text{dry}}(\text{RH} < 10\,\%)} \tag{2.1}$$

Where $\text{D}_{\text{wet}}(\text{RH})$ is the diameter of the aerosol particle for high relative humidity RH of approximately 90 %, and $\text{D}_{\text{dry}}(\text{RH} < 10\,\%)$ the particle's diameter in case of a relative humidity beneath 10 %.

Swietlicki et al. (2008), mentioned by Vu et al. (2021), describe a classification of hygroscopic properties of aerosols by their growth factor:

1. nearly-hydrophobic: $\text{Gf} \lesssim 1.11$

2. less-hygroscopic: $\text{Gf} \sim 1.11\text{-}1.33$

3. more-hygroscopic: $\text{Gf} \sim 1.33\text{-}1.85$

4. sea-salt aerosols: $\text{Gf} \gtrsim 1.85$

The size distribution of aerosol particles increases with relative humidity. In particular, Tang (1996) discovered, as can be read in Boucher (2015), that the relation of relative humidity and gain of size describes a hysteresis. A rapid growth appears for increasing humidity at the *deliquescence point*, due to transition of the solid to the liquid phase. For decreasing humidity there exists another critical point of rapid growth change, called the *efflorescence*

point (Boucher, 2015).

Zieger et al. (2013) defined another parameter for describing the modification of the particles' scattering effects as a function of relative humidity RH and wavelength λ. The *scattering enhancement factor* is

$$f(\text{RH}, \lambda) = \frac{\beta^{\text{aer}}(\text{RH}, \lambda)}{\beta^{\text{aer}}(\text{RH}_{\text{dry}}, \lambda)}$$

Where $\beta^{\text{aer}}(\text{RH}, \lambda)$ is the scattering coefficient at defined relative humidity RH and wavelength λ. And analogue, $\beta^{\text{aer}}(\text{RH}_{\text{dry}}, \lambda)$ is the dry scattering coefficient at dry conditions RH_{dry} and wavelength λ (Zieger et al., 2013). The scattering coefficient, that is obtained from lidar measurements, is further introduced in subsection 3.2. The relation between f and the relative humidity also takes the shape of a hysteresis.
f can be parameterized as

$$f(\text{RH}) = (1 - \text{RH})^{-\gamma} \tag{2.2}$$

with γ as *fit parameter* (Zieger et al., 2010). Zieger et al. (2010) and Gassó et al. (2000) used f for prediction of the hygroscopic growth. This method is called the *growth curve model*.

2.2. Seasonality and transport patterns: The Arctic haze

Anthropogenic aerosols as well as natural aerosols from distinct regions are transported into the Arctic. However, natural and anthropogenic aerosols follow a different annual cycle (Quinn et al., 2007). In addition, aerosols get to the Arctic via different possible routes (Stohl, 2006). The dominating source region of Arctic pollutants in winter is Eurasia, and for summer periods the North Atlantic ocean (Tunved et al., 2013). The variety of transport routes depends on the season. The duration of stay within the Arctic's atmosphere varies with season and altitude (Stohl, 2006).

Due to the variety of transport patterns, as well as the seasonality of aerosol sources, Arctic aerosol patterns are strongly fluctuating during one year. Nevertheless, they are predictable by means of their seasonality, transport processes and present meteorological conditions (Tunved et al., 2013).
According to Tunved et al. (2013), the Arctic year is divided into three main seasons with rapid transitions. The segmentation was made by means of differences in characteristics of aerosol populations, like concentration, chemical composition and transport ways.

1. The haze period (from March to May). The Arctic haze might also begin before March.

> For instance, Nielsen et al. (2019) investigated the Arctic haze phenomenon from February to May. In-situ measurements of Winiger et al. (2019) find the Arctic haze already to begin in December.

2. The sunlit summer (from June to August).

3. The remaining time of the year, starting in September.

Like done in this thesis, the annual cycle and seasonality of aerosols can be discussed by means of scattering and absorption effects (Tunved et al., 2013; Quinn et al., 2007). According to this, Quinn et al. (2007) and Tunved et al. (2013) locate the maximum of the Arctic haze in March and April. Concentrations of accumulation mode aerosols decrease during transition to summer months. Ström et al. (2009) state, as read in Tunved et al. (2013), that sunlit summer is characterized through formation of new, smaller particles. From September to February the Arctic atmosphere contains a lower amount of aerosols, with a minimum in September and October (Tunved et al., 2013).

The *Arctic haze* is described as a large accumulation of pollution from anthropogenic sources, which is transported into the Arctic and trapped there during winter and spring. Each pollutant stays there for about 15 to 30 days. The aerosols stem from industrialized regions in Europe, Asia and North America (Quinn et al., 2007). Important contributions to Arctic aerosols originate from biomass burning aerosols as boreal forest fire events became more frequent (Zielinski et al., 2020; Schmale et al., 2021; Warneke et al., 2010). Since 2009 it is known that forest fires are an important source for aerosols of the Arctic haze (Warneke et al., 2010). Biomass burning aerosols consist for example of black carbon, sulphates and nitrates, where anthropogenic sulphate is the most important contributor during the Arctic haze (Quinn et al., 2007). Moschos et al. (2022) pursued deeper research to the annual cycle of organic aerosols. They found them to coincide with the annual cycle of the Arctic haze. However, organic aerosols are only present in small amounts (Quinn et al., 2007).

Sulphates and organic aerosols cause a cooling effect at the surface, whereas the black carbon warms it due to absorption of solar radiation (Rinke et al., 2004). Penner et al. (2003) state, as mentioned by Rinke et al. (2004), that the magnitude of the warming effect is dependent on the particles' altitude. Even more so, there exists the possibility for a cooling effect. According to Rinke et al. (2004), the Arctic haze has high spatial fluctuation. Therefore it generates an additional cooling or warming effect that is dependent on its region.

The influences of natural aerosols, as well as of anthropogenic aerosols, on the Arctic are predicted to change by reason of global warming and diminished pollution in industrialized regions. These modifications of the aerosols' impact on the radiative budget are still a topic of research (Schmale et al., 2021).

Impacts of the haze cloud to its surrounding regions are generally a reduced visibility, altered radiative balance and negative consequences for the Arctic ecosystem (Quinn et al., 2007).

2.3. Scattering processes of aerosols

Depending on the ratio of particle radius r and incoming wavelength λ one has to distinguish between different types of scattering in the atmosphere: The *particle scattering*, and the *Raman* (inelastic) and *Rayleigh* (elastic) scattering. Raman and Rayleigh scattering occur for wavelengths much smaller than the size of the scattering particle. The scattering process is called particle scattering for similar magnitudes of wavelength and particle size (Roedel and Wagner, 2018). The particle size parameter $x = 2\pi \cdot \frac{r}{\lambda}$ is a measure of this ratio of wavelength λ and particle circumference r (Roedel and Wagner, 2018; Boucher, 2015).

Roedel and Wagner (2018) provide further information to these scattering processes. A short outline will be given.

The intensity of elastic Rayleigh scattered light is dependent on the wavelength λ of incoming radiation, by λ^{-4}, and for unpolarised light on its irradiation angle θ, by $1 + \cos(\theta)^2$. Incoming light induces oscillation of one of the electrons in the molecule, following the principles of a Hertzian dipole. This leads to emission of radiation that is referred to as Rayleigh scattered light. Thereby the wavelength stays unchanged regarding the incoming light (Roedel and Wagner, 2018).

The inelastic Raman scattering spectrum includes *Stokes* and *Anti-Stokes lines*. Scattered light increases or decreases in wavelength, referring to the wavelength of the incoming radiation (Demtröder, 2016). According to Roedel and Wagner (2018), only 2-4% of molecular scattering processes are Raman scattering.

The Mie theory (Mie, 1908) is used for calculation of scattering and absorption properties of particle scattering on spherical aerosols of arbitrary size. Furthermore, Mie theory includes Rayleigh scattering processes (Weitkamp, 2006). Mie scattering mostly results in forward scattering, due to its low irridation angle dependency. The size parameter and refractive index define this characteristics (Roedel and Wagner, 2018; Boucher, 2015).

The scattering and absorption behaviour of non-spherical particles do not follow the Mie theory. Whether Mie theory can be used for the present atmosphere has to be evaluated by means of depolarisation. Non-spherical particles depolarise the backscattered light, while spherical particles do not. For example ice crystals and aerosols like mineral dust are classified as non-spherical particles (Weitkamp, 2006).

3. Data and methods

In the following, the general construction of a lidar device is explained. Moreover the mathematical analysis of the lidar, and the derivation of corresponding formulars, is summarized. This analysis method, implemented in Matlab, was used for the investigation in this thesis. Additional information on the data set and its evaluation are given afterwards.

3.1. Measurement devices - lidar and radiosonde measuring

'Light Detection and Ranging', short lidar, is a high-resolved remote sensing technique. Lenoble et al. (2013) state the lidar to be one of only a few devices for obtaining vertically resolved aerosol measurements in lower and middle atmospheric levels. Lidar devices are subdivided into three categories depending on their state and place of measurement: There are ground-based, air-born and space-born lidar systems (Lenoble et al., 2013). The ground-based lidar will be discussed further in this section.

A lidar consists of three main parts: A laser, a telescope and an analyzing system. First, the laser emits short light pulses of $\sim 10\,\text{ns}$ with a wavelength between $250\,\text{nm}$ and $11\,\mu\text{m}$ (Weitkamp, 2006). After that, the light pulses often pass a beam widening system (Foken, 2021). The laser beam then heads towards the atmosphere, where aerosols and air molecules scatter it. A telescope receives the fraction of the light that was backscattered and forwards it to an analyzing system. This system consists of filter devices for polarization and wavelength, a detector and a computer. First, the backscattered light is directed to the filters. They facilitate the investigation of specific wavelengths and polarization states. After passing the filters, the remaining light is directed to the detector. Last but not least the resulting detector signal is passed to the computer. In conclusion, a lidar signal is a height-resolved profile of the light that is backscattered by aerosols and air molecules (Weitkamp, 2006).

The *overlap* of the lidar is defined as that region, where the field of view of the telescope completely displays the emitted laser beam. It start above the overlap height (Foken, 2021).

The data used in this thesis was obtained by the *Koldewey Aerosol Raman Lidar* (KARL) of the AWIPEV station in Ny-Ålesund, Svalbard (78°55'24"N, 11°55'15"E). It operates at the three wavelengths $355\,\text{nm}$, $532\,\text{nm}$ and $1064\,\text{nm}$. Furthermore, a lidar signal at $355\,\text{nm}$ and

532 nm is resolved according to the polarization state of the backscattered light, hence parallel or perpendicular. The measurements reach up to the mid of the stratosphere (Hoffmann, 2011).
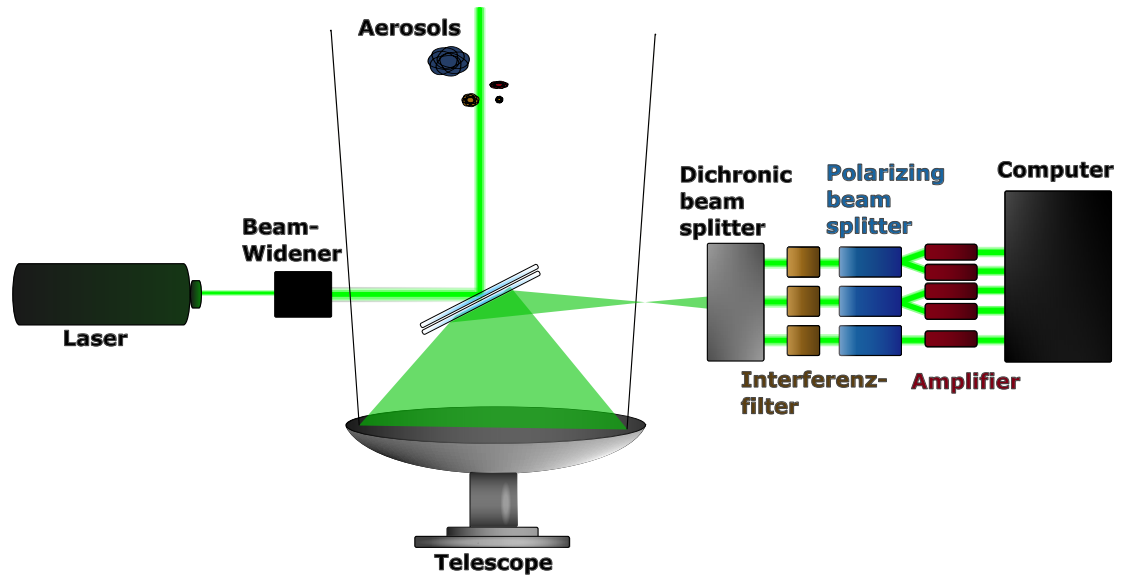
Figure 3.1.: A schematic construction of a backscatter lidar is illustrated. The emitted laser light undergoes a beam widening system, and is then directed to the atmosphere, where it is scattered in aerosols and air molecules. The backscattered fraction of light is collected via a telescope. Afterwards, it passes an analyzing system, where wavelength and polarization state are investigated. The resulting signal of the analysis is directed to a computer.

In comparison to lidar, in-situ devices do not measure from a distance, but directly at the location of the effect (Foken, 2021). For instance a radiosonde, whose data is also used in this thesis, is attached to a helium balloon and rises into the atmosphere. Variables like temperature, pressure, wind and humidity are measured while passing the air masses (NASA earth observatory). In this manner, profiles of air density or relative humidity can be obtained.

3.2. Analysis of backscatter lidar signals: The Klett method

The backscatter lidar provides a height-resolved profile. Information about aerosol and cloud properties can be obtained by evaluating, for example, polarization and intensity of the backscattered light.

The elastic lidar equation describes the height-resolved lidar signal $P(z)$. It is defined as:

$$P(z) = C\frac{1}{z^2}\beta(z)\exp\left(-2\int_{z_0}^{z}\alpha(\hat{z})\mathrm{d}\hat{z}\right) \tag{3.1}$$

Where, C is a constant that contains laser power, telescope area, transmission through all optical components and the quantum efficiency of the detector. $\frac{1}{z^2}$ serves as correction of the telescope range, $\beta(z)$ is the *volumetric backscatter coefficient* and $\alpha(z)$ is the *extinction coefficient*. Radiation passes the route between the particle and the laser twice. Hence, extinction occurs during both ways, leading to the term $-2\int_{z_0}^{z}\alpha(\hat{z})\mathrm{d}\hat{z}$ in equation 3.1. However, the elastic lidar equation does not hold for multiple scattering.

Via rearrangement of equation 3.1 on can define the range-corrected lidar signal $S(z)$.

$$S(z) := P(z)z^2 = C\beta(z)\exp\left(-2\int_{z_0}^{z}\alpha(\hat{z})\mathrm{d}\hat{z}\right) \tag{3.2}$$

Backscattering can occur on aerosols and other particles in the atmosphere. Subsection 2.3 introduced the scattering properties of aerosols and air molecules. Therefore, one distinguishes between backscattering on aerosols β^{aer} and Rayleigh scattered light on other particles β^{Ray}. The overall backscatter coefficient is defined as sum of these contributions

$$\beta := \beta^{\mathrm{aer}} + \beta^{\mathrm{Ray}} \tag{3.3}$$

Radiation is extinguished due to absorption α^{absorp}, and extinction through aerosols α^{aer} and air molecules α^{Ray}. In total, the extinction coefficient is written as

$$\alpha := \alpha^{\mathrm{aer}} + \alpha^{\mathrm{Ray}} + \alpha^{\mathrm{absorp}} \tag{3.4}$$

Klett (1981) provides a method to solve the elastic lidar equation, commonly known as the *Klett method*. Thanks to this method, a backscatter profile $\beta(z)$ is obtained: The *Klett solution*. A short outline will be discussed in this section. Foken (2021) discusses the derivation of the Klett solution in detail.

First, two preparatory steps need to be stated:

1. The backscatter coefficient β and the extinction coefficient α are assumed to correlate with the wavelength through a power-law. The corresponding exponent is the *Ångström exponent* $A_{a,b}$. The exponent depends on the particle size and takes values between -4 and 0. The lower boundary is called the *Rayleigh limit* for small particle, and the upper limit is the *gray approximation* for large particles. The power-laws are

$$\alpha^{aer} = C_1 \lambda^{A_a} \tag{3.5}$$

$$\beta^{aer} = C_2 \lambda^{A_b} \tag{3.6}$$

   With constants C_1 and C_2 (Ångström, 1964).

2. A new quantity is introduced. The *lidar ratio*

$$LR = \frac{\beta^{aer}}{\alpha^{aer}} \tag{3.7}$$

   leads to a connection between extinction and backscatter. Herein, molecular absorption α^{absorp} is minimized via choice of laser wavelength. Inserting equation 3.3 and 3.4 in equation 3.7 provides

$$\alpha = \alpha^{aer} + \alpha^{Ray} = LR(\beta - \beta^{Ray}) + \alpha^{Ray} \tag{3.8}$$

In-situ measurements of the density are consulted to obtain α^{Ray} and β^{Ray} because they are proportional to the air density (Bucholtz, 1995).

By means of the preparatory work, hence equations 3.5, 3.6 and 3.8, a *Bernoulli differential equation* is derived:

$$\frac{d\beta}{dz} = \left[\frac{d}{dz}(\ln S(z)) + 2(\alpha^{Ray} - LR\beta^{Ray}) \right] \beta(z) + 2LR(z)\beta^2(z)$$

where $S(z)$ is the range-corrected lidar equation from equation 3.2. To solve the Bernoulli equation boundary conditions are necessary. The backscatter value $\beta(z_{ref})$ at a specific height z_{ref} and the lidar ratio $LR(z_{ref})$ have to be estimated.

The final Klett solution is stated in equation 3.9

$$\begin{aligned}
\beta(z) &= \frac{\frac{S(z)}{S(z_{\mathrm{ref}})}\mathrm{ST}(z)}{\frac{1}{\beta(z_{\mathrm{ref}})} + \frac{2}{S(z_{\mathrm{ref}})}\int_z^{z_{\mathrm{ref}}} \mathrm{LR}(\tilde{z})S(\tilde{z})\mathrm{ST}(\tilde{z})\mathrm{d}\tilde{z}} \\
&= \frac{s(z)\mathrm{ST}(z)}{\frac{S(z_{\mathrm{ref}})}{\beta(z_{\mathrm{ref}})} + 2\int_z^{z_{\mathrm{ref}}} \mathrm{LR}(\tilde{z})S(\tilde{z})\mathrm{ST}(\tilde{z})\mathrm{d}\tilde{z}}
\end{aligned} \tag{3.9}$$

Where, $\mathrm{ST}(z) = \exp\left(-2\int\limits_z^{z_{\mathrm{ref}}}(\alpha^{\mathrm{Ray}} - \mathrm{LR}\cdot\beta^{\mathrm{Ray}})\mathrm{d}\hat{z}\right)$.

The Klett solution in equation 3.9 is numerical stable due to the integration from the top to the ground.

The quality of this solution depends on the chosen boundary condition $\beta^{\mathrm{aer}}(z_{\mathrm{ref}})$ and lidar ratio $\mathrm{LR}(z_{\mathrm{ref}})$, as well as on the lidar signal P_{λ_0}. A refinement of the explained method minimizes the possibility of inappropriate boundary conditions for measurements at multiple wavelengths. Furthermore, this modified approach is used in the thesis. Then, instead of choosing $\beta(z_{\mathrm{ref}})$ for each wavelength, one must only assume the Ångström exponent and a boundary condition ϵ for one wavelength. $\beta(z_{\mathrm{ref}})$ is calculated via

$$\beta(z_{\mathrm{ref}}) = (1 + \epsilon)\beta^{\mathrm{Ray}}(z_{\mathrm{ref}})$$

The boundary conditions of the remaining wavelengths can be calculated out of this $\beta(z_{\mathrm{ref}})$ by means of the assumptions 3.5 and 3.6 (Foken, 2021).

Ansmann et al. (1992) introduced a method to determine the aerosol extinction α^{aer} and backscatter β^{aer} independently from one another. The inelastically Raman backscattered lidar signal $P_{\lambda_{\mathrm{R}}}$ in equation 3.10 is to be established for this method. Note that the Raman effect of nitrogen molecules is observed here.

$$P_{\lambda_{\mathrm{R}}}(z) = C_{\mathrm{R}}\frac{1}{z^2}\beta^{\mathrm{Ray}}\exp\left(-\int_{z_0}^z [\alpha_{\lambda_0}(\hat{z}) + \alpha_{\lambda_{\mathrm{R}}}(\hat{z})]\mathrm{d}\hat{z}\right) \tag{3.10}$$

Herein, $\alpha_{\lambda_{0,\mathrm{R}}} = \alpha_{\lambda_{0,\mathrm{R}}}^{\mathrm{aer}} + \alpha_{\lambda_{0,\mathrm{R}}}^{\mathrm{mol}}$, i.e. the sum of extinction coefficient for elastic and inelastic scattered light. They arise from contributions of extinction by aerosols and air molecules. Note that the extinction forth and back is different because of the change in frequency. Therefore, in comparison to equation 3.1, one integrates over the sum of α_{λ_0} and $\alpha_{\lambda_{\mathrm{R}}}$. Since the Raman effect of nitrogen molecules is observed here, one can simplify equation 3.10 by replacing the Raman backscatter coefficient β^{Ray} with the number of nitrogen molecules in the atmosphere

N_R, due to their proportionality in the theory of the homosphere (Roedel and Wagner, 2018). Rearranging the inelastic lidar equation 3.10 results in equation 3.11 for $\alpha_{\lambda_0}^{\mathrm{aer}}$.

$$\alpha_{\lambda_0}^{\mathrm{aer}} = \frac{\frac{\mathrm{d}}{\mathrm{d}z}\left[\ln \frac{N_R(z)}{P_{\lambda_R}(z)z^2}\right] - \alpha_{\lambda_0}^{\mathrm{mol}}(z) - \alpha_{\lambda_R}^{\mathrm{mol}}(z)}{1 + \left(\frac{\lambda_0}{\lambda_R}\right)^{A_a}} \tag{3.11}$$

A_a equals 1 for aerosols and water droplets of sizes similar to the wavelength of the laser (Ansmann et al., 1992).

Besides, nitrogen number N_R as well as the extinction and backscatter coefficients α^{mol} and β^{mol} are obtained by radiosonde data. The method of Ansmann et al. (1992) provides equation 3.12 for the backscatter coefficient $\beta_{\lambda_0}^{\mathrm{aer}}$.

$$\begin{aligned}
\beta_{\lambda_0}^{\mathrm{aer}}(z) = & -\beta_{\lambda_0}^{\mathrm{mol}}(z) + [\beta_{\lambda_0}^{\mathrm{aer}}(z_0) + \beta_{\lambda_0}^{\mathrm{mol}}(z_0)] \\
& \times \frac{P_{\lambda_0}(z)P\lambda_R(z_0)N_R(z)}{P_{\lambda_0}(z_0)P_{\lambda_R}(z)N_R(z_0)} \\
& \times \frac{\exp\left(-\int_{z_0}^{z}[\alpha_{\lambda_R}^{\mathrm{aer}}(\hat{z}) + \alpha_{\lambda_R}^{\mathrm{mol}}(\hat{z})]\mathrm{d}\hat{z}\right)}{\exp\left(-\int_{z_0}^{z}[\alpha_{\lambda_0}^{\mathrm{aer}}(\hat{z}) + \alpha_{\lambda_0}^{\mathrm{mol}}(\hat{z})]\mathrm{d}\hat{z}\right)}
\end{aligned} \tag{3.12}$$

In recent studies, measurements at multiple wavelengths and a polarisation analysis of the backscattered light are frequently utilized. By this, further information of the aerosols' size and shape are gathered. The two corresponding quantities are shortly introduced hereafter. The color ratio

$$\mathrm{CR} = \frac{\beta_{355\,\mathrm{nm}}^{\mathrm{aer}}}{\beta_{532\,\mathrm{nm}}^{\mathrm{aer}}} \tag{3.13}$$

is a size that is composed of the backscatter of two different wavelengths, herein 355 nm and 532 nm. A decrease in color ratio implies a growth of particles. The pure dependence on size results from scattering properties regarding specific wavelengths. The color ratio of small particles is such as $\left(\frac{355}{532}\right)^{-4}$ due to the proportionality of Rayleigh scattering to λ^{-4}. In comparison, the color ratio becomes 1 for big particles, because the upper limit is almost constant regarding the laser wavelength (Foken, 2021).

By consideration of the polarisation of the backscattered light, one gets information about the state of aggregation of particles. The aerosol depolarisation is defined via the parallel polarised

backscatter signal $\beta_{\parallel}^{\text{aer}}$, and $\beta_{\perp}^{\text{aer}}$ as the perpendicular polarised backscatter (Foken, 2021):

$$\delta^{\text{aer}} = \frac{\beta_{\perp}^{\text{aer}}}{\beta_{\parallel}^{\text{aer}}} \tag{3.14}$$

Mie theory states that spherical particles, like water droplets, do not cause a change in polarisation (Mie, 1908). Further information on scattering processes can be found in section 2.3.

3.3. The lidar data set and further information to its processing

In this thesis lidar data from April 2021 to the end of July 2021 is investigated. The data has a spatial resolution of 7.5 m and temporal resolution of 10 minutes. Since tropospheric aerosol is to be examined, the research contains only data of up to 10 km. In addition, only data above 0.7 km is discussable, as this is the *overlap height*. The overlap is mentioned in subsection 3.1.

Available time steps undergo a filter that controls the impact of clouds on the lidar signal. If a cloud influences the time step, the backscatter signal takes too high values. The cloud filter rejects all time steps that consist of a *backscatter ratio* $\text{BSR}(\lambda) = 1 + \frac{\beta^{\text{aer}}(\lambda)}{\beta^{\text{Ray}}(\lambda)}$ bigger than 4. After the cloud mask, 451 lidar measurements, out of 1046, remain. For the following analysis in sections 4 and 5 only filtered data is used, unless stated otherwise.

The 31st of July 2021 is marked by the presence of optical thick clouds. According time steps got filtered out by the cloud mask. Since these cloud formations are to be analysed, the investigation of time steps with cloud influence is needed. The boundary conditions in the clouds need to be adapted manually for this single day. An alternative to the correction of the boundary conditions is used here because the cloud influence only shifted the backscatter profiles systematically. For adjustment of the measurements, the backscatter is linearly multiplied towards backscatter values of time steps with fewest cloud influence.

If time steps of other days include no optical thick clouds, but small cloud influence, it might be necessary to adapt the lidar ratio within the cloud. At the position of the optical thin cloud, the lidar ratio is automatically adopted, like in Nakoudi et al. (2021).

On occasion, a separation into different height intervals is done in sections 4 and 5. Müller (2019) and Rader (2020) use similar intervals.

Often, the median upon specific height or time intervals is calculated. In contrast to the mean, the median is more stable towards fluctuations, and captures the average value better for a non-symmetrical distribution.

4. Results

In this section significant results of the investigation are presented and analyzed. Firstly, the development of physical aerosol properties is discussed by means of the optical parameters such like backscatter, depolarisation and color ratio. Afterwards, the general hygroscopic behaviour is investigated. Trends of hygroscopic growth with respect to height and season are gathered for the whole time period of April to July. Subsequent, individual hygroscopic growth events are further discussed by analysis of single days. In particular, first non-hygroscopic behaviour, and then highly fluctuating cloud layers are examined.

4.1. Seasonal trends in physical aerosol properties

The research looks at backscatter, extinction, depolarisation, lidar ratio and color ratio profiles from April 2021 to end of July 2021. A daily median is built and illustrated for discussion of the temporal development of physical aerosol properties. First, the backscatter is evaluated, and afterwards the extinction, depolarisation, lidar ratio and color ratio.

4.1.1. Backscatter

Figure 4.1 displays the temporal evolution of the daily median backscatter for the wavelength 532 nm. The median was calculated between 0.7 km and 10 km. Strong variability in backscatter appears through the months, hence a variability in e.g. aerosol concentration and composition.

The median backcatter shows an undulating structure till mid of May. It rises by almost 50 % to its maximum in mid May. This leads to the hypothesis that the Arctic haze might appear till mid or end of May in the year 2021. Furthermore, the maximum in May is the overall maximum of figure 4.1 and amounts to $0.2 \, \mathrm{Mm^{-1}sr^{-1}}$. The daily median backscatter then halves rapidly till mid of June. From the beginning of July, it starts to rise again. The minimum median backscatter is $0.052 \, \mathrm{Mm^{-1}sr^{-1}}$. The 31st of July 2021 deviates from other values in July. The day is further discussed in a case study in subsection 4.3.2.
It remains unknown if the maximum of the Arctic haze already appeared in March.

Because of e.g. transport patterns through different heights the Arctic aerosols are expected to vary within altitude. Figure 4.2 compares the daily median backscatter of the height intervals
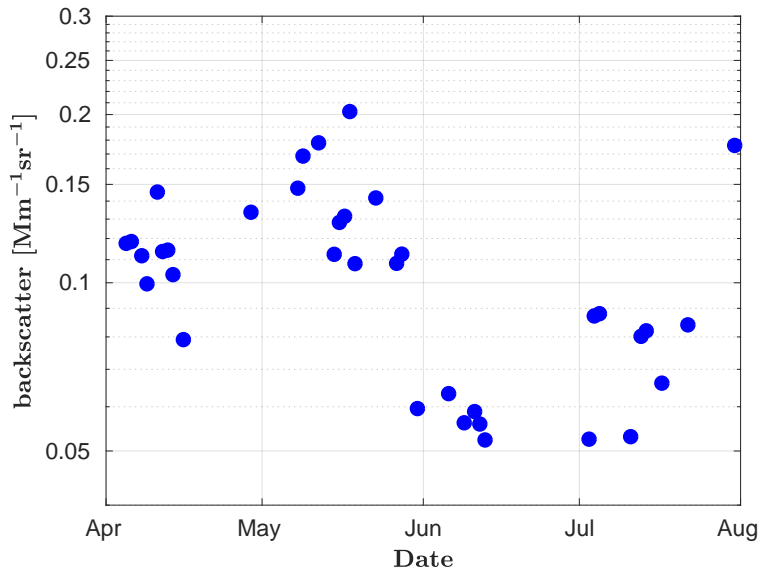
Figure 4.1.: Temporal development of the daily median backscatter from April to July 2021. The median was built from $0.7 - 10\,\text{km}$. The backscatter rises in May to the overall maximum. It lowers till mid of June. Afterwards, the median backscatter rises again during July.

$0.7 - 2.5\,\text{km}$ (a) and $2.5 - 4.5\,\text{km}$ (b). The data point of the 31st of May represents an exception, due to a very clear atmosphere.

The median backscatter of the lower height interval is highly fluctuating during April, May and June. Data points differ in ranges of approximately $0.2\,\text{Mm}^{-1}\text{sr}^{-1}$ or $0.3\,\text{Mm}^{-1}\text{sr}^{-1}$. In July, the fluctuation of the median backscatter decreases to approximately $0.05\,\text{Mm}^{-1}\text{sr}^{-1}$.

In contrast, the median backscatter of the upper height interval scatters less. The magnitude of variation in April and May is about $0.1\,\text{Mm}^{-1}\text{sr}^{-1}$. Beginning in June, the fluctuation decreases as well to approximately $0.05\,\text{Mm}^{-1}\text{sr}^{-1}$.

The median backscatter developments of figures 4.2a and 4.2b look alike till June, though the transition from spring to summer is more visible in the upper height interval. As of July, the increase is only visible in the upper height interval. The median backscatter in the lower height interval stays almost constant.

Regarding the magnitude of the backscatter, the interval $0.7 - 2.5\,\text{km}$ usually shows higher backscatter values than the interval $2.5 - 4.5\,\text{km}$. From April to May the median backscatter is approximately $0.32\,\text{Mm}^{-1}\text{sr}^{-1}$, whereas the median backscatter of the second height interval is $0.13\,\text{Mm}^{-1}\text{sr}^{-1}$. This is about 59% lower. In June and July the backscatter of the lower height interval is by median $0.22\,\text{Mm}^{-1}\text{sr}^{-1}$. Yet the median backscatter of the upper height interval is $0.069\,\text{Mm}^{-1}\text{sr}^{-1}$, thus approximately 31% of the median backscatter from the lower height interval. Overall, the daily median backscatter values of height interval $0.7 - 2.5\,\text{km}$

19

Figure 4.2.: The temporal development of the daily median backscatter of intervals $0.7 - 2.5\,\mathrm{km}$ (a) and $2.5 - 4.5\,\mathrm{km}$ (b) are illustrated. The time period ranges from April to July 2021. The Arctic haze in terms of backscatter values is most pronounced in the lower height interval. Nevertheless, the annual cycle with the transition polluted to clear is more apparent in the upper height interval.

reach up to $0.52\,\mathrm{Mm}^{-1}\mathrm{sr}^{-1}$ in April and May, and the ones of the height interval $2.5 - 4.5\,\mathrm{km}$ to $0.24\,\mathrm{Mm}^{-1}\mathrm{sr}^{-1}$. Likewise, the maximum value $0.11\,\mathrm{Mm}^{-1}\mathrm{sr}^{-1}$ between June and July for the upper height interval is as well smaller than the maximum value $0.38\,\mathrm{Mm}^{-1}\mathrm{sr}^{-1}$ of this period for the lower height interval.

Additionally, figure 4.3 and figure 4.4 illustrate the daily median backscatter of the height intervals $4.5 - 6.5\,\mathrm{km}$ and $6.5 - 10\,\mathrm{km}$. The correlation in temporal development and fluctuation of the median backscatter of all four height intervals is the strongest between $2.5 - 4.5\,\mathrm{km}$ in figure 4.2b and $4.5 - 6.5\,\mathrm{km}$ in figure 4.3. Therefore, they look similar to the overall median of $0.7 - 10\,\mathrm{km}$ in figure 4.1. The increase in summer has the same extent for the two height intervals. Yet it is more visible in $4.5 - 6.5\,\mathrm{km}$, due to lower variation in June. The median backscatter in higher altitudes of $6.5 - 10\,\mathrm{km}$ in figure 4.4 is more constant and weaker through out the seasons than for the other height intervals. From April to May the median backscatter is $0.092\,\mathrm{Mm}^{-1}\mathrm{sr}^{-1}$, and during June and July $0.056\,\mathrm{Mm}^{-1}\mathrm{sr}^{-1}$. The median backscatter of the highest height interval $6.5 - 10\,\mathrm{km}$ amounts to $25 - 29\,\%$ of the lowest height interval $0.7 - 2.5\,\mathrm{km}$. The progression is almost constant till May. The decrease from May to June is visible, yet of lower gradient. In July the increase is of same magnitude as for $2.5 - 4.5\,\mathrm{km}$ and $4.5 - 6.5\,\mathrm{km}$. This rise in summer is visible in all three height intervals $2.5 - 4.5\,\mathrm{km}$, $4.5 - 6.5\,\mathrm{km}$ and $6.5 - 10\,\mathrm{km}$. A hypothesis is that forest fire impacts on the upper troposphere cause this increase.
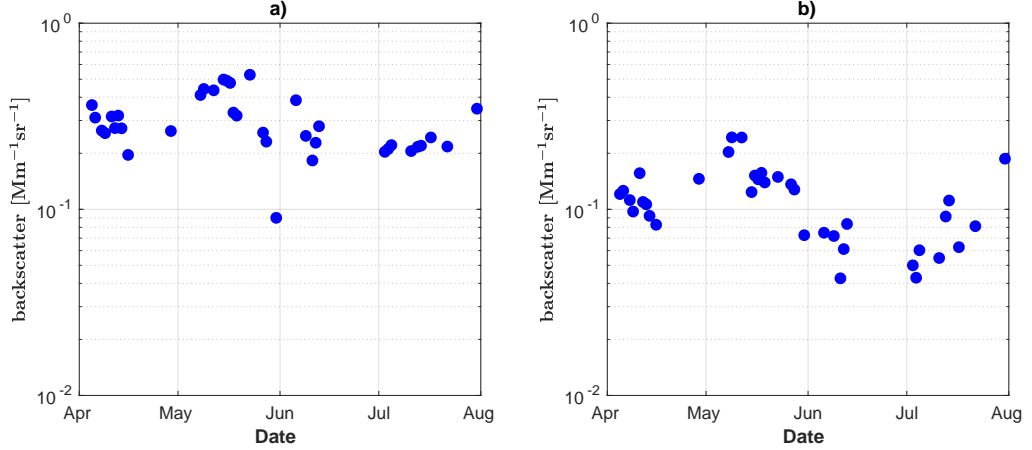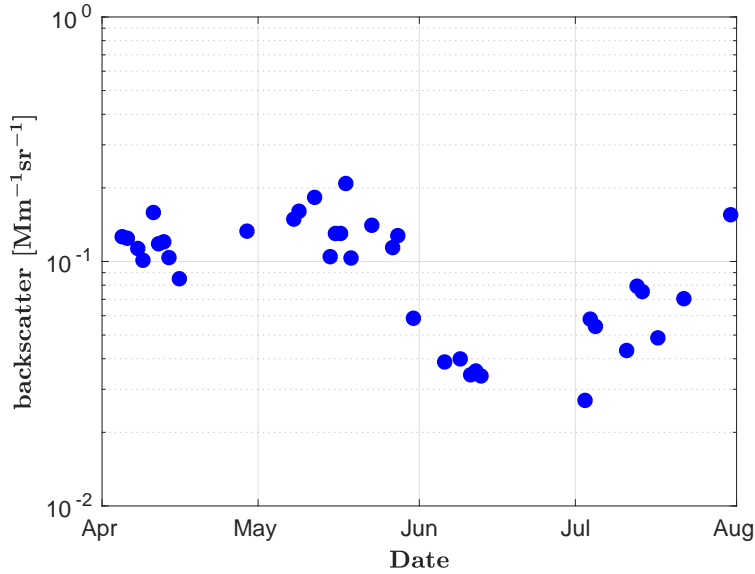
Figure 4.3.: The temporal development of the daily median backscatter from April to July 2021 is displayed. The median was built from $4.5\,km$ to $6.5\,km$. Similar trends as for the interval $2.5 - 4.5\,km$ are visible, but the summer development of the aerosols is more pronounced. This increase in July might stem from forest fire aerosols that are transported within the upper troposphere.
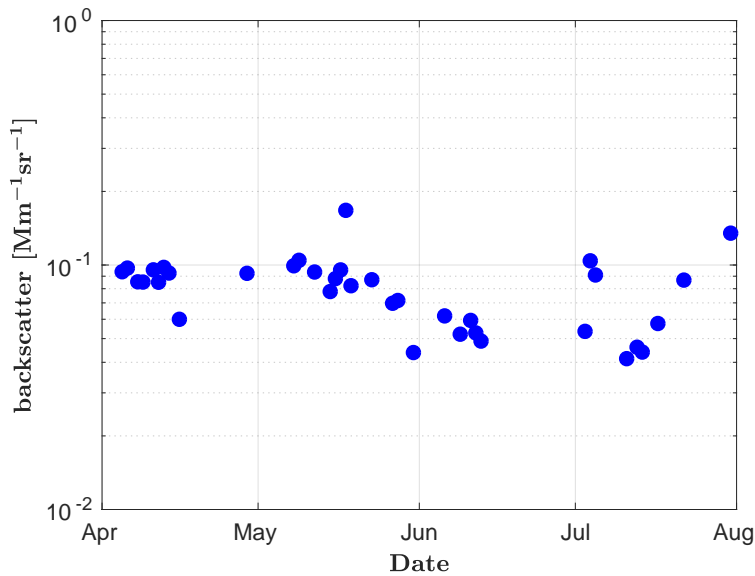
Figure 4.4.: The temporal development of the daily median backscatter from April to July 2021 is displayed. The median was built from $6.5\,km$ to $10\,km$. No influence of the Arctic haze is present from April to May. The backscatter progression is almost constant. It then decreases from May to June. The increase of backscatter in July is still visible. It might stem from forest fire aerosols that are transported within the upper troposphere.

High backscatter is considered as a synonym for Arctic haze in this analysis of the Arctic spring. Therefore, the lower altitudes consist of stronger Arctic haze than upper altitudes, thus more aerosols. Nevertheless, the transition from Arctic haze to the clearer summer season is most pronounced between 2.5 km and 6.5 km.

Table A.1 in the Appendix displays the 25th, 50th and 75th percentiles of the backscatter by month and height. Previously discussed trends visible, i.e. two facts: The table illustrates that the backscatter values and fluctuations decrease with altitude. The reduction of backscatter in transition from May to June is visible, too.

Covered by Arctic haze pollution, a *background* can be classified as clearest conditions of the month at certain altitude. By consideration of figures 4.1 to 4.4 one can define a backscatter of less than $0.1 \, \mathrm{Mm^{-1}sr^{-1}}$ as a *clear* condition. Higher values are considered as *pollution*, and thus Arctic haze in spring and forest fire impacts in summer.

A summary of recent findings is given. The backscatter rises from April to mid of May. Whether aerosols of May belong to the Arctic haze or not needs to be investigated in the following subsections. The backscatter decreases till June and increases afterwards. The haze in terms of backscatter values is the strongest in the lower altitudes. Despite this, the transition of Arctic haze to summer season is most pronounced between 2.5 km and 6.5 km.

4.1.2. Extinction
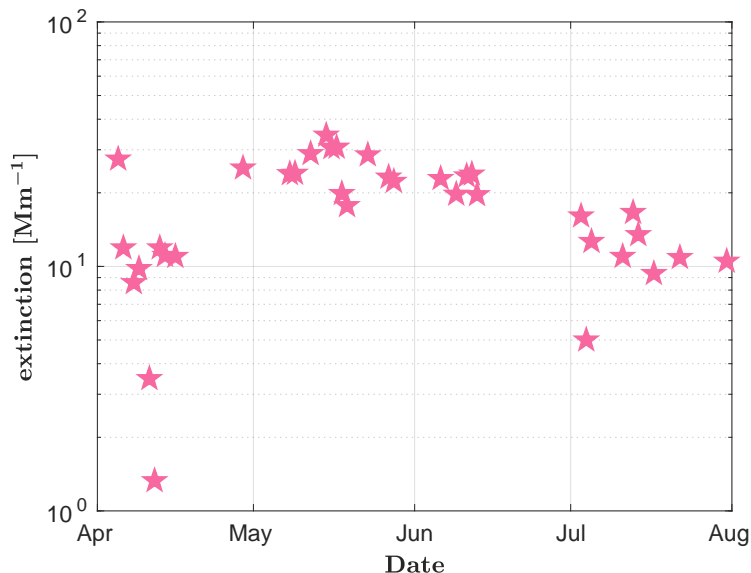
Figure 4.5.: The daily median extinction of the height interval $0.7 - 2.5$ km is displayed from April to July 2021. After the maximum in May, the extinction decreases.

The median extinction of height interval $0.7 - 2.5\,\text{km}$ is displayed in figure 4.5. Height intervals above $2.5\,\text{km}$ exhibit too much noise in extinction, as shown in figure B.1. The median extinction of $0.7 - 2.5\,\text{km}$ rises to its maximum in mid of May. Afterwards it decreases continuously. The values of the 11th and 12th of April stand out with low values. This results from a clear atmosphere.

4.1.3. Aerosol depolarisation
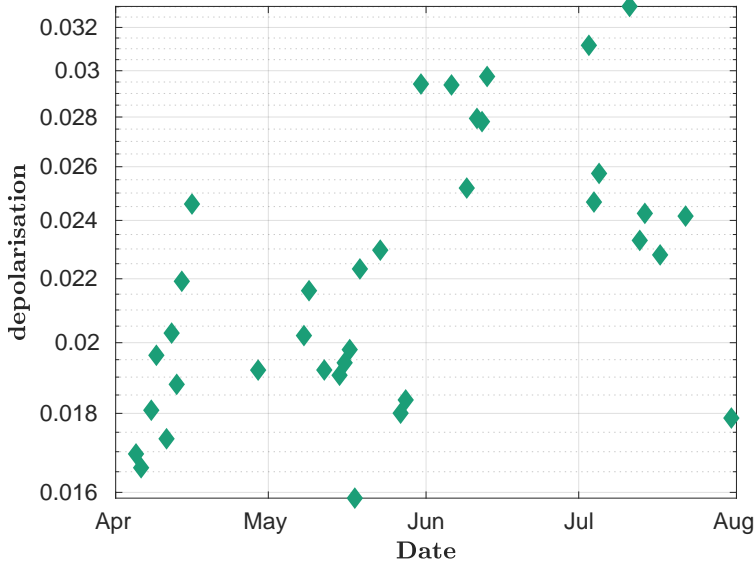
Figure 4.6.: The temporal development of the daily median aerosol depolarisation is illustrated from April to July 2021. The median is built upon $0.7 - 10\,\text{km}$. Due to low values of $2\,\% - 3\,\%$, the aerosols are mostly spherical through out the period.

The daily median aerosol depolarisation of height interval $0.7 - 10\,\text{km}$ is illustrated in figure 4.6. The depolarisation does not vary much through out the period and takes values of $2 - 3\%$. Therefore, the aerosols are mostly spherical.

4.1.4. Lidar ratio

The lidar ratio is influenced by the noise of the extinction, according to equation 3.7. Hence, solely the lidar ratio of $0.7 - 2.5\,\text{km}$ is displayed in figure 4.7. Large fluctuations are visible in April and July. The 31st of May is not displayed, due to its unreasonable values. In April the lidar ratio varies between approximately $20\,\text{sr}$ to $50\,\text{sr}$, except for the 11th and 12th of April. The lidar ratio is higher and more constant in May and early June. Around mid-June, it then rises further to values of up to $90\,\text{sr}$. Enhanced lidar ratios generally indicate either strongly absorbing or small, elongated particles (Foken, 2021). Here, elongated particles can be ruled
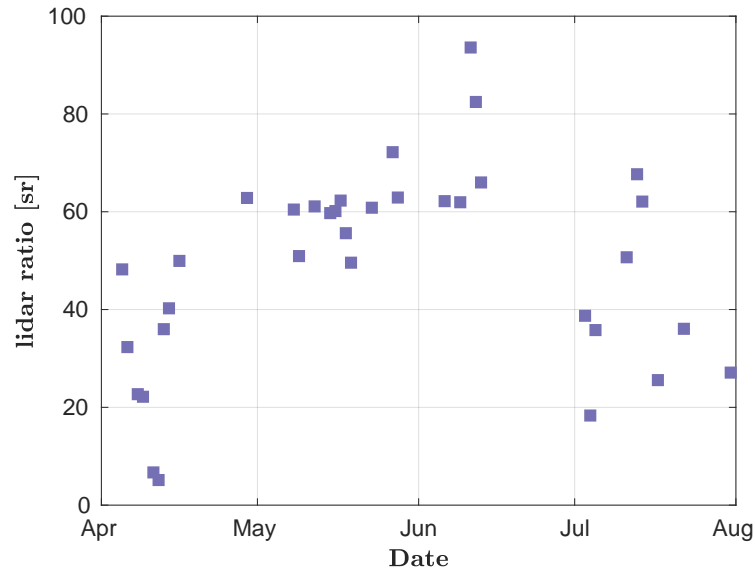
Figure 4.7.: The daily median lidar ratio from April to July 2021 is displayed. Likewise to the extinction, only the height interval $0.7 - 2.5\,\mathrm{km}$ can be considered, due to noise. The 31st of May is not shown because of unphysical values. The lidar ratio indicates an extended haze season till May, however interrupted in April. Forest fire impacts are visible in July.

out, due to the overall small values in the depolarisation, see figure 4.6.

The enhanced lidar ratio from May to early June implies a higher refractive index than in April. In combination with the maximum values of extinction and backscatter it indicates that the haze season in 2021 peaked in May, hence slightly later in the season than expected. The variability of backscatter and lidar ratio in April shows that during this month the Arctic haze period was clearly interrupted around mid April. Especially on 11th and 12th of April a very clear atmosphere has been found, leading to low extinction, hence low lidar ratios. The high lidar ratio in June and occasionally in July could potentially be explained by forest fire aerosol with a high amount of black carbon.

Careful use of the lidar ratio of figure 4.7 is necessary, due to high noise in extinction and partially not plausible lidar ratios for April and June. However, extinction in May in figure 4.5 shows no high fluctuations.

4.1.5. Color ratio

The size of aerosols is discussed by means of the color ratio. Figure 4.8 displays the daily median color ratio of height interval $0.7 - 10\,\mathrm{km}$. It continuously rises from April to July and amounts to approximately two or three. Thus the aerosols become smaller through out the period. The
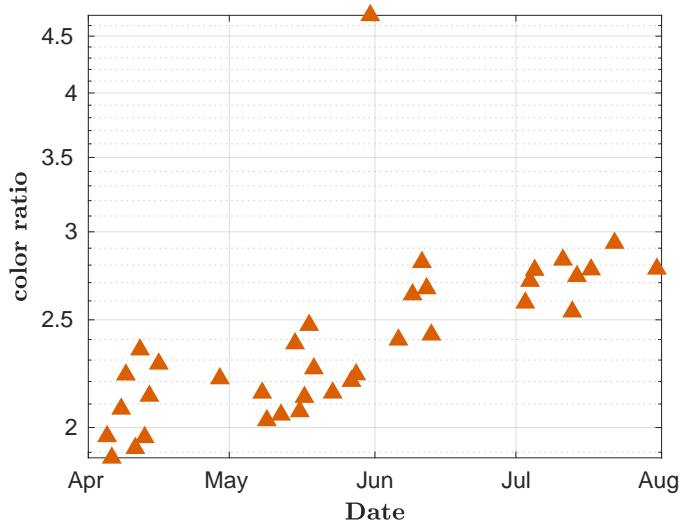
Figure 4.8.: The daily median color ratio from April to July 2021 is displayed. The median was built from 0.7 km to 10 km. Particle sizes decrease through out the season. This is shown by the rise in color ratio. The 31st of May consists of a very clear atmosphere and represents an exception to the trend.
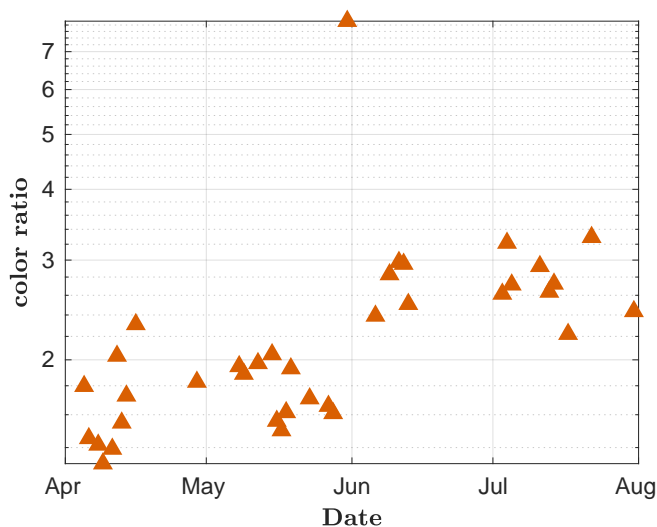
Figure 4.9.: The daily median color ratio from April to July 2021 is displayed. The median was built from 0.7 km to 2.5 km. It indicates a decrease in particle size in transition to summer, hence beginning in June. In combination with the increased lidar ratio in May (see figure 4.7) the aerosols of May are identified as Arctic haze pollution.

31st of May represents an exception again, due to previously mentioned circumstances of a clear atmosphere. Because the color ratio is calculated according to equation 3.13 the value

becomes unstable for low backscatter, resulting in these extreme values.

Figure 4.9 shows the development of median color ratio for the height interval $0.7 - 2.5\,\mathrm{km}$. It shows a decrease in particle size in transition to summer, too. As mentioned before, the aerosol accumulation in May is likely to be pollution from the haze period. The enhanced particle size in May stresses this hypothesis.

To conclude, the aerosols get smaller through out the observed time period. In particular, the lowest height interval contains larger aerosols of similar sizes in April and May. The aerosols of May stem from haze pollution, too.

4.2. Hygroscopicity of the aerosols from April to July 2021

For investigation of hygroscopic growth, one assumption has to be made. It is assumed that the physical aerosol properties do not change strongly within one height interval of the free troposphere. In the free troposphere, i.e. above $2.5\,\mathrm{km}$, in general old aerosols from long-range transport are observed. In combination with wind shear there is no strong gradient in aerosols' microphysical properties. Then hygroscopic growth is indicated by the relation of physical aerosol properties and relative humidity. Changes in backscatter, color ratio and depolarisation, that are observed parallel to strong humidity gradients, are interpreted to stem from hygroscopic behaviour of the aerosols. Validity and gain of this hypothesis remain to be investigated in future studies.

Filtered data was used for this analysis, hence no clouds are contained in the measurements. The comparison of backscatter and relative humidity is performed only with lidar measurements which took place ± 30 minutes with respect to the launch of the radiosonde. Therefore, 33 out of 451 lidar profiles remain for this study.

Figure 4.10a displays the backscatter with respect to the relative humidity over water and 4.10b with respect to the relative humidity over ice. A separation of relative humidity in these two categories is necessary. Since every aerosol can act as *cloud condensating nuclei* (CCN) at sufficient humidity, but not as *ice nucleating particles* (INP), relative humidity over water is defined in ranges of $0\,\%$ and $100\,\%$ while relative humidity over ice can be greater than $100\,\%$. If hygroscopic growth would be indicated, figure 4.10a would show a strong increase of backscatter starting at $40\,\%$ relative humidity over water (Zieger et al., 2010). Instead, large scatter is present in the plot. The median backscatter for each percentage of relative humidity is displayed in figures 4.10a,b to illustrate an average trend.
On average, the Arctic aerosols pursue a hygroscopic behaviour. The median backscatter increases with relative humidity in figure 4.10. The rise at relative humidity lower than $40\,\%$ stems from natural fluctuations because no hygroscopic growth is expected for this dry circumstances (Zieger et al., 2010). The median backscatter gets chaotic for a relative humidity
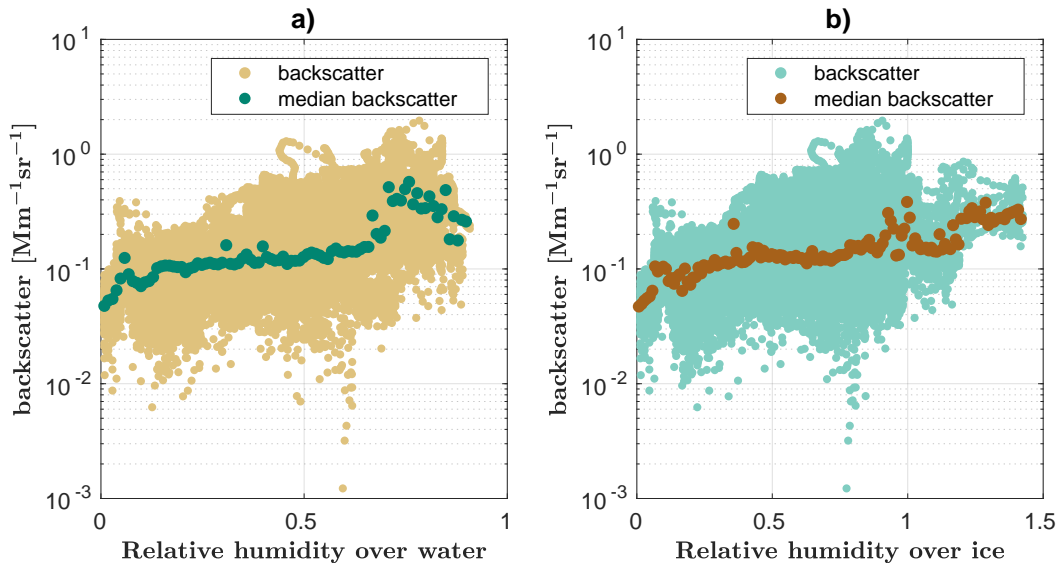
Figure 4.10.: The scatter plot illustrates all time steps from April to July 2021, which went through the cloud filter. The backscatter is plotted against the relative humidity over water (a) and over ice (b), respectively. In addition, the median backscatter for each percentage is plotted. It demonstrates that the aerosols generally follow a hygroscopic behaviour. Below 40 % and above 70 % relative humidity over water natural fluctuations dominate.

higher than 70 %. To conclude, the development of the median backscatter shows the average hygroscopic behaviour of Arctic aerosols only in between 40 % and 70 % relative humditiy over water. An increase by $0.06\,\mathrm{Mm^{-1}sr^{-1}}$ is seen in this interval.

Figure 4.10b exhibits a chaotic behaviour above 120 % relative humidity over ice.

The chaotic behaviour of figure 4.10a,b above 70 % relative humidity over water or rather 120 % over ice either stems from cloud formations, because they happen rapidly and thus lead to an offset of radiosonde and lidar, or from INP. However, in general the development of figures 4.10a,b at those wet circumstances demonstrates that individual case studies need to be examined to understand this variability. It takes place in subsection 4.3.

For future research, figure 4.10 might be important for climate modelling as well, since the backscatter as function of humidity can be gained between 40 % and 70 % relative humidity over water. A growth curve, according to equation 2.2, is applied in figure 4.11 for the normalized median backscatter between 40 % and 70 % relative humidity over water. The normalization is performed by division with a reference median backscatter value for dry conditions, hence the median between $0-40\,\%$ relative humidity over water. A fit parameter of approximately $\gamma = 0.47$ suits the data. By assuming that disruptive effects average out, due to the variety of cases and heights, this fit parameter is equivalent to a seasonal average.
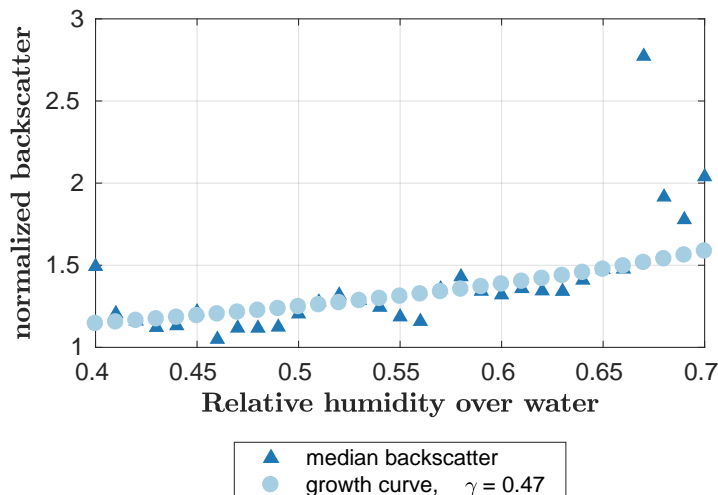
Figure 4.11.: The normalized median backscatter from April 2021 to July 2021 between 0.7 km and 10 km for humidity interval $40 - 70\%$ relative humidity over water is illustrated. The normalization is made by division with a dry reference value of the backscatter. This reference is obtained between $0 - 40\%$ relative humidity over water. A growth curve with parameter $\gamma = 0.47$ is fitted on the data. Such a growth curve might be used for a simplified description of the average hygroscopic growth of Arctic aerosol.

Figure 4.12a displays the backscatter with respect to the relative humidity over water and 4.12b to the relative humidity over ice. The scatter plots are colored according to the height of the scattering particle in the atmosphere. They range from $0.7 - 10$ km.

Trends in heights are present. The highest backscatter of $1.9 \, \mathrm{Mm}^{-1}\mathrm{sr}^{-1}$ appears in the lower 3 km of the atmosphere at oversaturated relative humidity. Higher altitudes of $8 - 10$ km show smaller backscatter than these lower altitudes. The backscatter amounts merely between $10^{-2} \, \mathrm{Mm}^{-1}\mathrm{sr}^{-1}$ to $0.9 \, \mathrm{Mm}^{-1}\mathrm{sr}^{-1}$, depending on relative humidity. Intermediate heights show the same magnitudes as the higher altitudes.

The upper heights show a chaotic behaviour at high relative humidity over ice in figure 4.12b, too. Due to the low temperatures around $-40\,°\mathrm{C}$ in the upper troposphere, one only has to consider the relative humidity over ice. But there do exist less INP than CCN, hence leading to higher variability in the upper troposphere.

Figure C.1 in the Appendix is similar, but contains a colormap according to the date. April is the most dryest month, or other data points are covered. In May high backscatter values are often to be found at increased relative humditiy.

For further investigation, percentiles are examined: Table 4.1 shows the 25th, 50th and
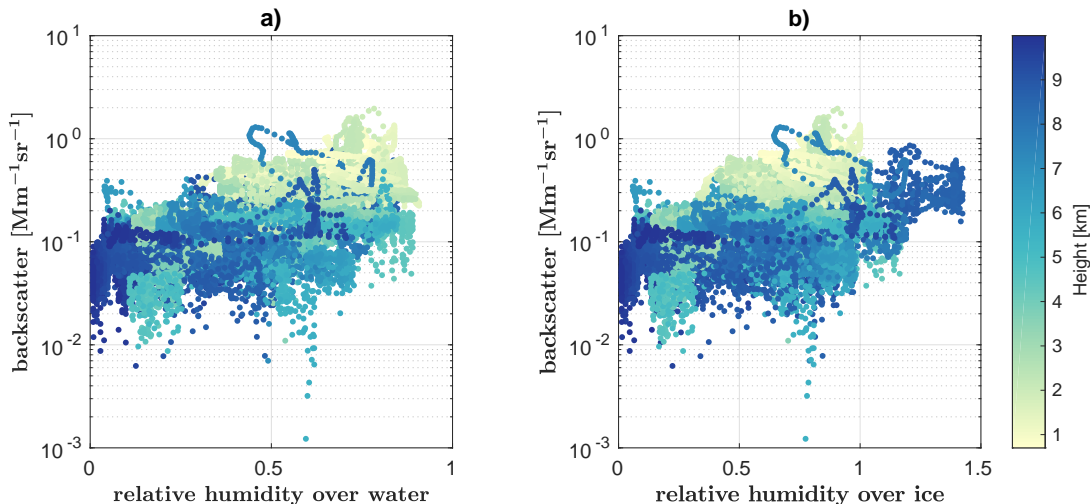
Figure 4.12.: The scatter plot illustrates all time steps between $0.7 - 10\,\text{km}$ from April to July 2021, that pass the cloud filter. The backscatter is plotted against the relative humidity over water (a) and over ice (b), respectively. The color map is height-resolved. Usually lower altitudes provide high backscatter at oversaturated relative humidity over water.

0.7 - 10 km				
percentile	April	May	June	July
0.25	0.3057	0.3283	0.2199	0.3651
0.50	0.4393	0.4917	0.4308	0.6200
0.75	0.5469	0.6279	0.6059	0.7214
0.7 - 2.5 km				
percentile	April	May	June	July
0.25	0.3643	0.5058	0.5321	0.6744
0.50	0.4637	0.6948	0.5923	0.7287
0.75	0.6100	0.7628	0.7350	0.8159
6.5 - 10 km				
percentile	April	May	June	July
0.25	0.1986	0.1917	0.0877	0.2500
0.5	0.3125	0.3392	0.3959	0.3238
0.75	0.4400	0.4655	0.5695	0.4443

Table 4.1.: The 25th, 50th and 75th percentile of relative humidity are gathered by month and height interval. Two general trends are visible. The first observation is that the relative humidity decreases with altitude. The second observation regards the seasonality. May and July consist of a more humid troposphere than April and July.

75th percentile of the relative humidity over water of different height intervals and months. Together with table A.1 in the Appendix, further information to time and height dependent hygroscopic behaviour can be obtained. The relative humidity varies strongly with height and

season, according to table 4.1. Regarding a height dependent trend, one can see that humidity decreases with height, in general. A seasonal analysis of table 4.1 indicates that overall May and July show higher humidity values than April and June. The corresponding backscatter in table A.1 shows that often, May consists of the highest backscatter values. The seasonal backscatter trend is like discussed in section 4.1.

Via comparison of these two tables, it is visible that the percentiles of humidity are similar for May and July 2021. At the same time, the backscatter in May generally seems to be slightly higher than in July. This corresponds with findings of figure C.1 where May consists of enhanced backscatter parallel to high humidity values. Since the hygroscopic behaviour in May and summer season seems to differ, one can make the hypothesis of different aerosol species. The hypothesis of Arctic haze pollution in May is stressed.

In conclusion, the Arctic aerosols show an average hygroscopic behaviour, like illustrated by figure 4.10. A rise of backscatter with humidity was determined between 40 % and 70 % relative humidity over water in figure 4.10a. Seasonal modifications of hygroscopic growth as well as a height dependent trend are visible. Lower altitudes consist of higher backscatter values parallel to higher humidity. Via comparison of seasonal trends in backscatter and humidity, one can see that May 2021 generally consists of higher backscatter than July for similar relative humidity. This difference lies in accordance with the hypothesis of an Arctic haze event in May, in comparison to the aerosols' summer trend in July.

4.3. Case studies regarding hygroscopicity of Arctic aerosols

Subsection 4.2 dealt with a general analysis of the hygroscopic growth between April and the end of July 2021. There is not just one hygroscopic growth trend for all days. Already Rinke et al. (2004) stated, the aerosols' radiative effect, hence physical properties, to depend on current atmospheric conditions. Therefore, two individual days are discussed in the following to examine aerosol hygroscopic behaviour with respect to current meteorological conditions. The first case study treats non-hygroscopic behaviour of aerosols, and the second case study the high variability of multiple cloud layers. In particular, a rare ice cloud is observed in the second case study.

The analysing procedure is the following:
In particular, backscatter, aerosol depolarisation and color ratio are discussed parallel to strong humidity gradients. The backscatter increases, when aerosols grow due to water uptake. Color ratio indicates the size of a particle, but since it is defined as division of two backscatter signals from different wavelengths (see equation 3.13), it might suffer from enhanced noise. For instance, similar, low backscatter values might result in an unreasonable high or low color ratio.

Therefore, backscatter profiles provide a more stable first analysis of hygroscopicity than color ratio profiles. Instead of a first indication of hygroscopic growth, the color ratio is utilized for support of hypotheses of hygroscopic growth. The aerosol depolarisation agrees with the hypothesis of hygroscopic growth if it decreases. Due to water uptake the particles get more spherical.

4.3.1. Case study 1: Complications and difficulties of hygroscopic growth at the example of the 15th of May

The 15th of May 2021 is characterized by missing hygroscopic behaviour of some aerosols. The lidar data of 10:40:08 UTC is discussed here, because current trends are stressed and it is one of the temporally closest measurements to the radiosonde data of 10:46:10 UTC.

Figure 4.13.: The profiles of backscatter and relative humidity over water and ice of the 15th of May 2021 are displayed from $0.7\,\mathrm{km}$ to $10\,\mathrm{km}$. The lidar measurement took place at 10:40:08 UTC and the radiosonde measurement at 10:46:10 UTC. The strong humidity gradient from $5.6 - 7.1\,\mathrm{km}$ has no influence on the backscatter of the aerosols. It indicates non-hygroscopic behaviour.

Figure 4.13 displays the profiles of backscatter and relative humditiy. The temperature profile is shown in figure D.1 the Appendix. Above approximately $6\,\mathrm{km}$ the temperature is lower than $-35\,^\circ\mathrm{C}$. Only the relative humidity over ice is therefore relevant above $6\,\mathrm{km}$, and the relative humidity over water below $6\,\mathrm{km}$. Because INP are rare, it is assumed that above $-35\,^\circ\mathrm{C}$ the relative humidity over ice can be neglected.

From $7.1\,\mathrm{km}$ to $8.7\,\mathrm{km}$ a positive correlation between backscatter and humidity is visible. Likewise, from $2.0\,\mathrm{km}$ to $2.5\,\mathrm{km}$ the aerosols follow a subtle hygroscopic trend. Yet, neither the

strong humidity gradient in $5.6 - 7.1 \, \text{km}$ nor weak fluctuations in humidity from $2.5 \, \text{km}$ to $5.6 \, \text{km}$ seem to have an impact on the backscatter profile. In the following, the hygroscopicity of those intervals is investigated further.
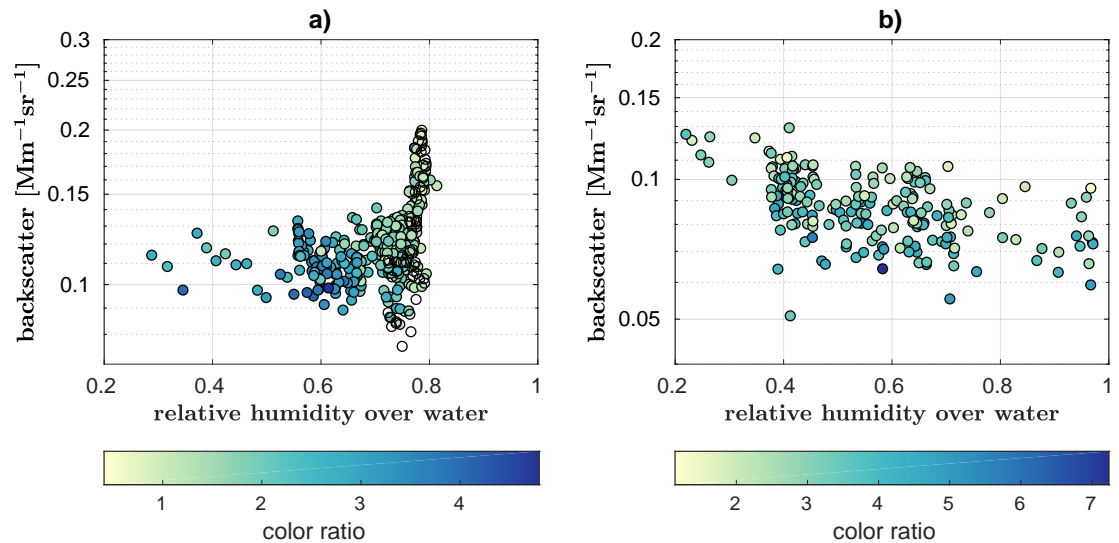
Figure 4.14.: The scatter plot illustrates the backscatter of the aerosols at certain relative humidity over water for the 15th of May 2021. Figure (a) displays the height interval $2.5 - 5.6 \, \text{km}$, and figure (b) $5.6 - 7.1 \, \text{km}$. Like expected, the upper height interval (b) shows no hygroscopic growth. Natural fluctuations dominate. Backscatter values of the lower height interval (a) increase with humidity. The color map depends on the color ratio. Hygroscopic growth of the lower height interval is indicated by the color ratio. By comparison, no correlation of backscatter and color ratio is present for the upper height interval.

The scatter plot in figure 4.14a underlines the small increase in backscatter with humidity of height interval $2.5 - 5.6 \, \text{km}$. The color map of this figure is based on the color ratio. It indicates larger particle size at enhanced humidity. The color ratio profile in figure 4.15 coincides with this results - color ratio increases while humidity decreases. Even the rise in humidity from $4.4 - 4.7 \, \text{km}$ might be visible in the color ratio profile. But no correlation of color ratio and backscatter is visible in figure 4.14a. For a certain relative humidity, high backscatter values come together with the same color ratio as for low backscatter values. But this color ratio development might also stem from fluctuations. Overall, a subtle hygroscopic trend is visible between $2.5 \, \text{km}$ and $5.6 \, \text{km}$.

The backscatter values of $5.6 - 7.1 \, \text{km}$ in figure 4.14b seem to decrease with humidity. Moreover, no correlation of color ratio with either backscatter or humidity is present. The aerosols are consistently small. The color ratio profile in figure 4.15 implies no correspondence of color
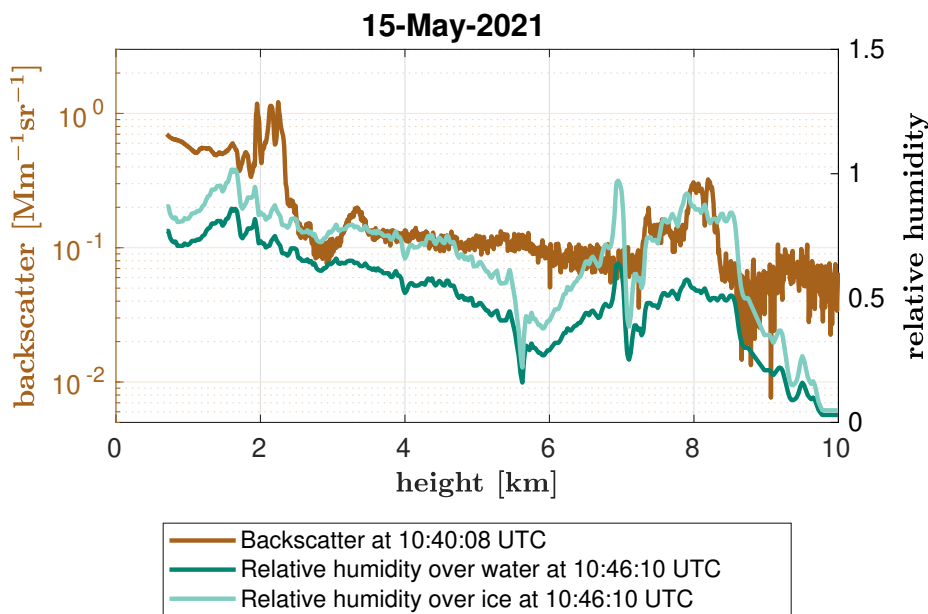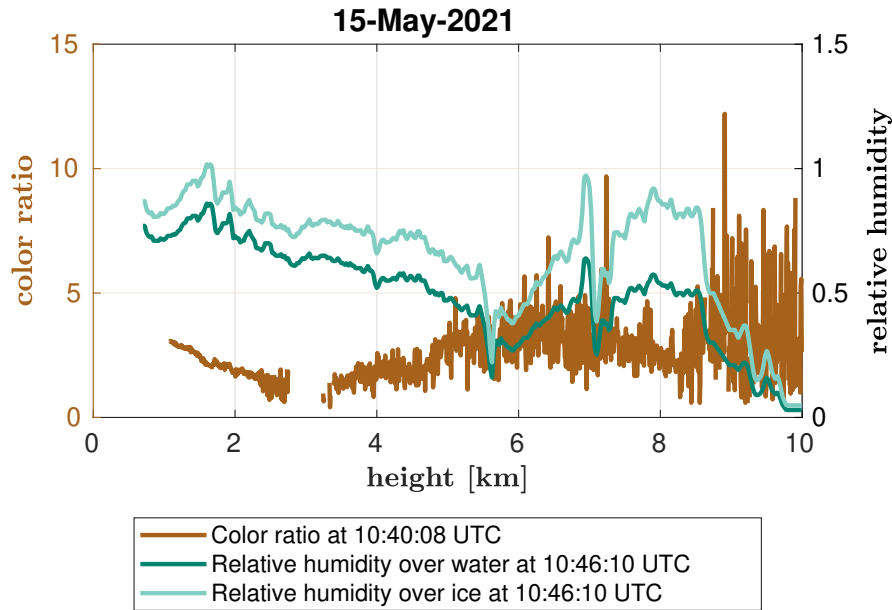
Figure 4.15.: The profiles of color ratio and relative humidity over water and ice of the 15th of May 2021 are displayed from 0.7 km to 10 km. The lidar measurement took place at 10:40:08 UTC and the radiosonde measurement at 10:46:10 UTC. Non-hygroscopic behaviour between 5.6 km and 7.1 km is indicated again. The particle growth does not follow the curve progression of increasing humidity. The lack at approximately 3 km height results from too low backscatter values. Since the color ratio is defined as division of two backscatter signals (see eq. 3.13), it might get extreme values for low backscatter. Therefore, no color ratio is calculated when the backscatter is low.

ratio and humidity developments, too.

Note that the relative humidity over ice is oversaturated, but since the depolarisation in figure 4.16 indicates no ice particles, the relative humidity over water was used for the analysis.

The scatter plot of depolarisation and backscatter in figure 4.17a shows a decrease in depolarisation parallel to an increase in backscatter. This might indicate hygroscopic growth. However, changes are small and no hygroscopic growth is demonstrated in the color ratio profile in figure 4.15. The trend therefore stems from fluctuations.

Overall, no hygroscopic growth appears between $5.6 - 7.1$ km, despite the strong humidity gradient.

The backscatter is high within the humidity gradient of $7.1 - 8.7$ km. Moreover, the color ratio and depolarisation in figures 4.15 and 4.16 are low. Growth of the aerosols is assumed for this height interval.

The depolarisation profile in figure 4.16 displays enhanced values above and below this interval. The scatter plots in figures 4.17a,b of backscatter and depolarisation of the intervals $5.6 - 7.1$ km (a) and $8.7 - 9.5$ km (b) show that backscatter increases if depolarisation decreases. Hygroscopic
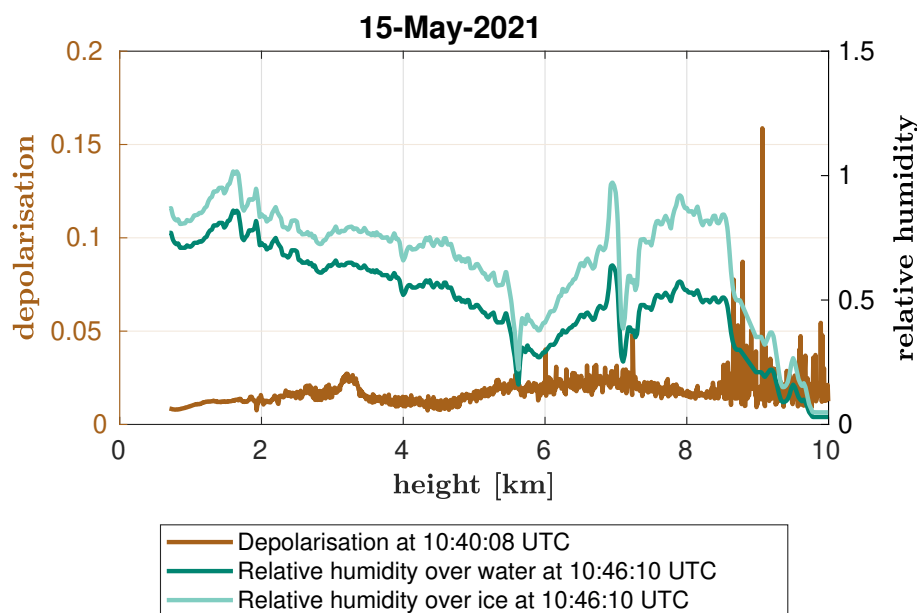
Figure 4.16.: The profiles of aerosol depolarisation and relative humidity over water and ice of the 15th of May 2021 are displayed from $0.7\,\mathrm{km}$ to $10\,\mathrm{km}$. The lidar measurement took place at 10:40:08 UTC and the radiosonde measurement at 10:46:10 UTC. Increased values are observed above $8.5\,\mathrm{km}$ and from $5.6\,\mathrm{km}$ to $7.1\,\mathrm{km}$. No hygroscopic growth is expected above $8.7\,\mathrm{km}$, because of the low temperature, and below $7.1\,\mathrm{km}$, due to previous results.
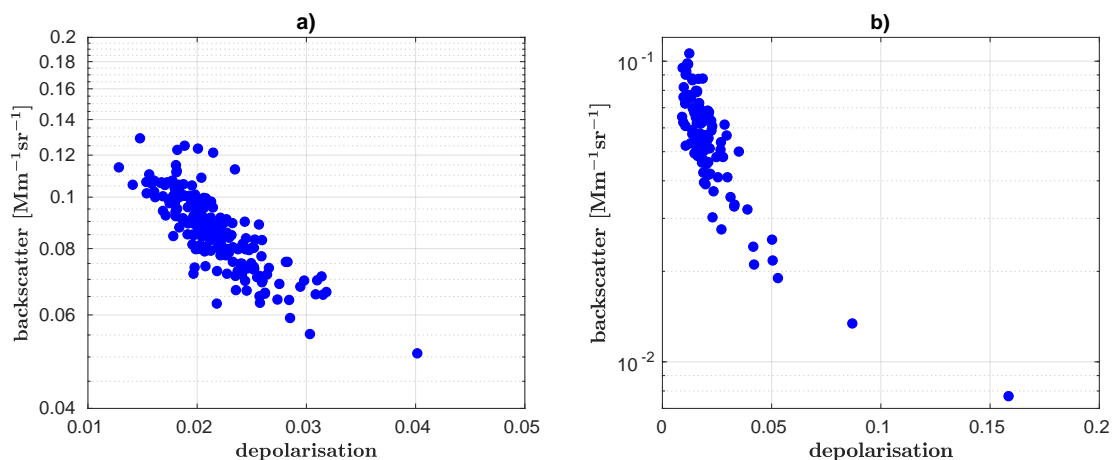
Figure 4.17.: The relation of backscatter and depolarisation from $5.6 - 7.1\,\mathrm{km}$ (a) and $8.7 - 9.5\,\mathrm{km}$ (b) for the 15th of May 2021 are displayed. The parallel decrease of depolarisation and increase of backscatter might indicate hygroscopic growth. However, depolarisation stays low and only takes values between $1\,\%$ and $4\,\%$. And since the color ratio profile of figure 4.15 does not imply a growth of the particles in interval $5.6 - 7.1\,\mathrm{km}$, hygroscopic growth is ruled out for this height.

growth due to water uptake leads to more spherical particles. Hygroscopic growth was ruled out for the interval $5.6 - 7.1 \, \text{km}$. Above $8.7 \, \text{km}$ the temperature is low, hence no water is present. Hygroscopic growth is therefore not expected above $8.7 \, \text{km}$, too. The enhanced backscatter values above $8.7 \, \text{km}$ might stem from ice particles. Despite this, the relative humidity over ice is low.

In conclusion, no clear hygroscopic behaviour is visible on the 15th of May 2021. From $5.6 - 7.1 \, \text{km}$ no hygroscopic growth occurs, despite strong humidity gradients. Other height intervals, i.e. $2.5 - 5.6 \, \text{km}$ and $7.1 - 8.7 \, \text{km}$, display hygroscopic behaviour partially. The composition of the aerosols is highly variable within altitude for this day.

4.3.2. Case Study 2: Multiple cloud layers with high temporal variability at the example of the 31st of July

The 31st of July 2021 was marked by the growth of multiple cloud layers, i.e. one ice cloud and two water clouds. The water clouds show high temporal variability. For observation of these cloud formations and their physical properties, the cloud mask is omitted.
The fourth backscatter profile of the lidar data from 10:59:23 UTC and the humidity profiles of the radiosonde from 10:49:03 UTC are shown in figure 4.18. The previous lidar measurement of 10:48:05 UTC is temporally closer to the start of the radiosonde balloon. However, by consideration of the balloons time of ascent, the fourth lidar measurement is temporally closer to the measured effects of the radiosonde.

Three events of high backscatter values at elevated humidity are present in figure 4.18. The lowest is located at at $3 - 3.9 \, \text{km}$, the next at $5.2 - 5.8 \, \text{km}$, and the highest cloud ranges from $8.5 \, \text{km}$ to $9.5 \, \text{km}$. The backscatter coefficient reaches values of up to $53 \, \text{Mm}^{-1}\text{sr}^{-1}$. The lowest two peaks of backscatter are slimmer than the corresponding humidity gradient. Yet, the highest event shows opposite slopes, the extent of the backscatter and the humidity peaks are of good correspondence.

The hypothesis is that these three backscatter peaks indicated three cloud layers. Their physical properties are investigated in the following with the figures 4.19, 4.20, and 4.21. They illustrate the backscatter, aerosol depolarisation and color ratio profiles of the third, fourth and fifth timestep of the day. Hence, they demonstrate the temporal development of the clouds' physical properties.

The upper height interval $8.5 - 9.5 \, \text{km}$ contains a relatively stable backscatter peak. It rises with time, but the order of magnitude stays nearly constant. Like seen before in figure 4.18, the backscatter peak coincides with the humidity peak. The relative humidity over ice is oversaturated. The occurrence of an ice cloud is possible, since the temperature profile in figure E.1 in the Appendix demonstrates that the temperature is low at this height interval.
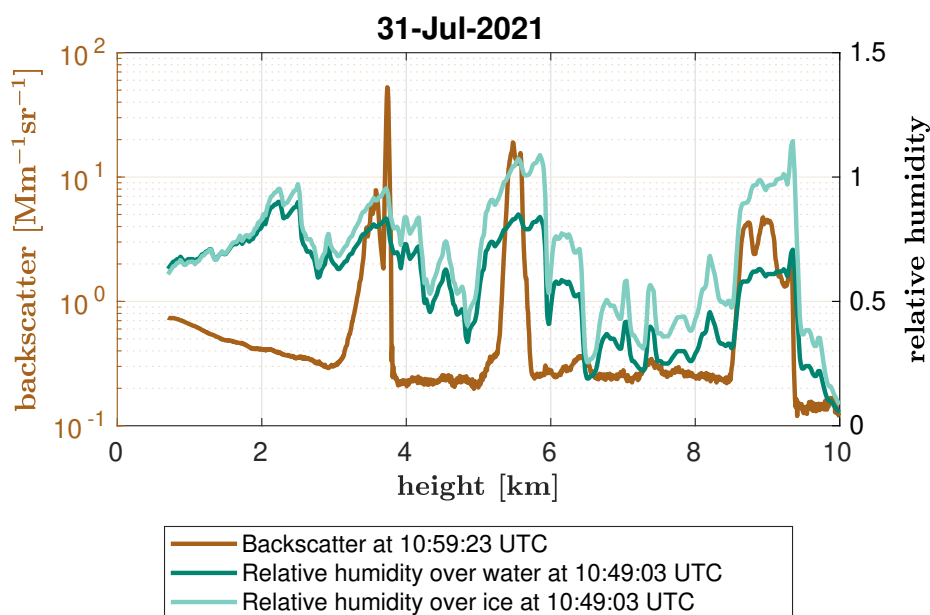
Figure 4.18.: The backscatter and relative humidity profiles from $0.7\,\mathrm{km}$ to $10\,\mathrm{km}$ on the 31st of July 2021 are displayed. The lidar measurement took place at 10:59:23 UTC and the radiosonde measurement at 10:49:03 UTC. Three parallel peaks of humidity and backscatter are visible: Firstly from $3.0 - 3.9\,\mathrm{km}$, secondly from $5.2 - 5.8\,\mathrm{km}$, and thirdly from $8.5 - 9.5\,\mathrm{km}$.

The color ratio profile in figure 4.21 indicates large particles between $8.5\,\mathrm{km}$ and $9.4\,\mathrm{km}$. High aerosol depolarisation is present, too. Figure 4.20 shows values of up to $22\,\%$. Ice particles are likely to be the cause of this. Therefore, the upper cloud is in fact an ice cloud, which is almost stable in time.

The backscatter peak of the intermediate height interval $5.2 - 5.8\,\mathrm{km}$ first increases and then decreases. The color ratio of the third and fourth time step is low between $5.0\,\mathrm{km}$ and $5.7\,\mathrm{km}$, while the color ratio of the fifth time step is of the same magnitude as in between the clouds. Only a small reduction is present for the interval $5.4 - 5.7\,\mathrm{km}$. The developments of the backscatter and color ratio profiles coincide, since the backscatter decreases for the fifth time step as the color ratio increases. It means that the particles get smaller and cause a decrease of the backscatter. The depolarisation in figure 4.20 displays a sharp decrease between $5.2\,\mathrm{km}$ and $5.8\,\mathrm{km}$, which implies more spherical particles. Overall, the intermediate cloud is a highly variable water cloud. Due to water uptake, the aerosols grow and get more spherical.

Note that the relative humidity over water is not oversaturated, still a water cloud forms. Because this water cloud has a short lifetime, i.e. begins to vanish in the fifth time step, measurement errors of the radiosonde with respect to the lidar measurement need to be taken into account. The measurement of the lidar and the radiosonde might not coincide completely. Recorded effects might differ due to the high temporal variability of the cloud.
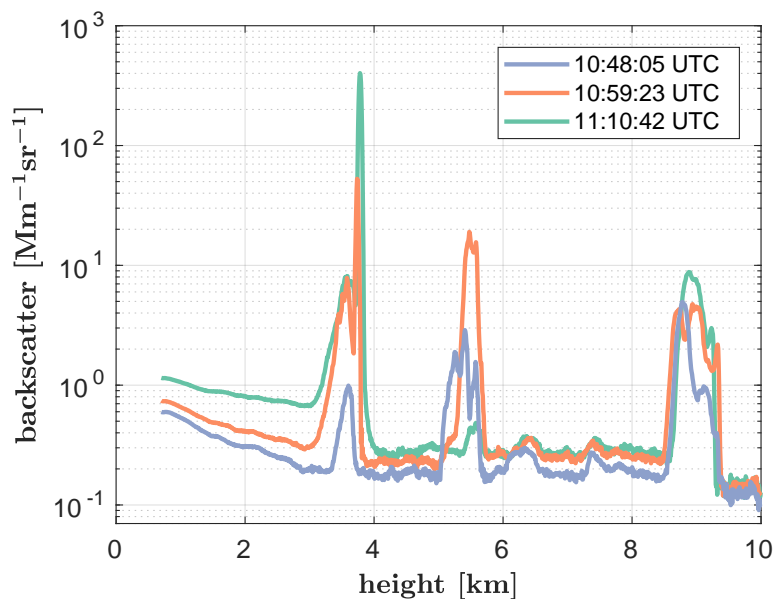
Figure 4.19.: Backscatter profiles from 11:10:42 UTC, 10:59:23 UTC and 10:48:05 UTC from the 31st of July 2021 are displayed. They illustrate the temporal development of the backscatter. In particular, the lower and upper peak rise with time, while the intermediate increases and then decreases. The lowest peak grows the most, by approximately two magnitudes.

The lower cloud grows with time. The backscatter peak between $3.0\,\text{km}$ and $3.9\,\text{km}$ in figure 4.19 increases strongly by two magnitudes. Natural cloud growth as well as unnatural mechanisms, like a *feeder-seeder effect* by the upper ice cloud, are possible causes of this strong backscatter growth. A feeder-seeder effect means that ice particles from the high ice cloud sink down to the lower cloud, and cause it to grow. This needs to be investigated in the following. The color ratio is low between $3.3\,\text{km}$ and $3.9\,\text{km}$. Large particles are present. By evaluation of the depolarisation in figure 4.20 a feeder-seeder effect can be ruled out. Despite the enhanced depolarisation at position of the lower cloud, the values are too small for ice particles. The small increase is only visible in the fourth and fifth time step. Since the backscatter is also extremely high for these two time steps, this rise in depolarisation is probably caused by multiple scattering. Multiple scattering interferes with the Mie theory, and might lead to those enhanced depolarisation values. Therefore, no ice particles are present at the lower cloud. Instead it is a water cloud, that grows strongly with time.

For further research of the hygroscopic behaviour of the aerosols, the relation of backscatter to humidity has to be investigated. The lidar measurement of 10:59:23 UTC is considered for this. The three observed events differ, hence various hygroscopic behaviours are expected. Therefore, these events are investigated individually in figures 4.22 and 4.23.
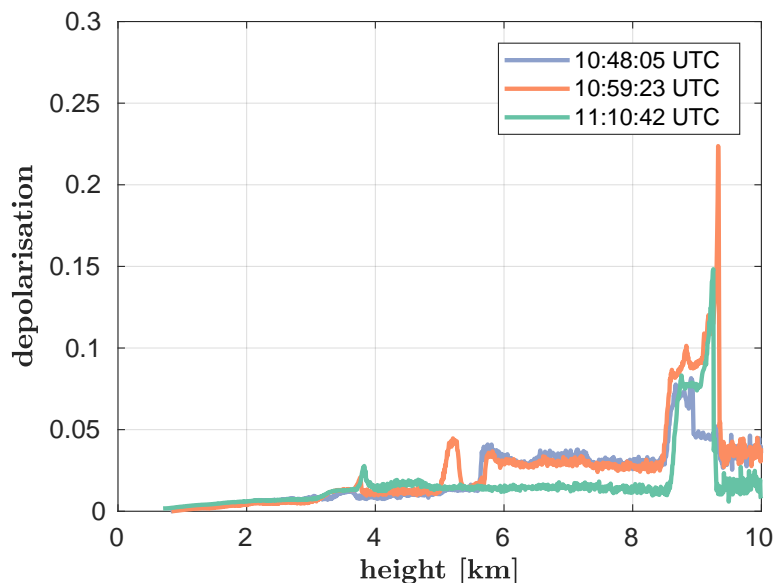
Figure 4.20.: Aerosol depolarisation profiles from 11:10:42 UTC, 10:59:23 UTC and 10:48:05 UTC from the 31st of July 2021 are displayed. They illustrate the temporal development of the depolarisation. Enhanced depolarisation values are visible between 8.5 km and 9.4 km, thus at position of the upper cloud. From 5.4 km to 5.7 km the depolarisation is low. A small rise is visible approximatley at the position of the lower cloud. Therefore, the upper cloud is likely to be an ice cloud, and the lower and intermediate clouds are water clouds. The enhanced depolarisation of the lower cloud stems from multiple scattering.

The upper ice cloud in figure 4.22 provides two different backscatter progressions. The first one begins to rise at 47 % relative humidity over ice. The second development increases later, hence at 100 % relative humidity over ice. The two progressions coincide with the inconsistent backscatter peak in figure 4.18. This peak contains smaller fluctuations. Therefore, the backscatter sometimes rises and sometimes decreases with relative humidity. The highest relative humidity does not coincide with appearance of the maximal backscatter. Nevertheless, the overall relation is a rise of backscatter with humidity. The color ratio is displayed by means of the color map. A decrease in color ratio appears simultaneously with a rise of backscatter, meaning that the particles grow. It coincides with previous results. The minimal color ratio amounts to approximately one, which is the limit of big particles. In particular, by comparison of the two trends in figure 4.22 it is visible that enhanced backscatter values at same humidity comes parallel to increased particle size. The occurrence of hygroscopic growth is stressed.
The lower and intermediate clouds are displayed in figure 4.23. The lower cloud in figure 4.23a follows an almost linear relation between backscatter and humidity for low and medium humidity. From a relative humidity over water of 77 %, the progression gets more chaotic. In addition,
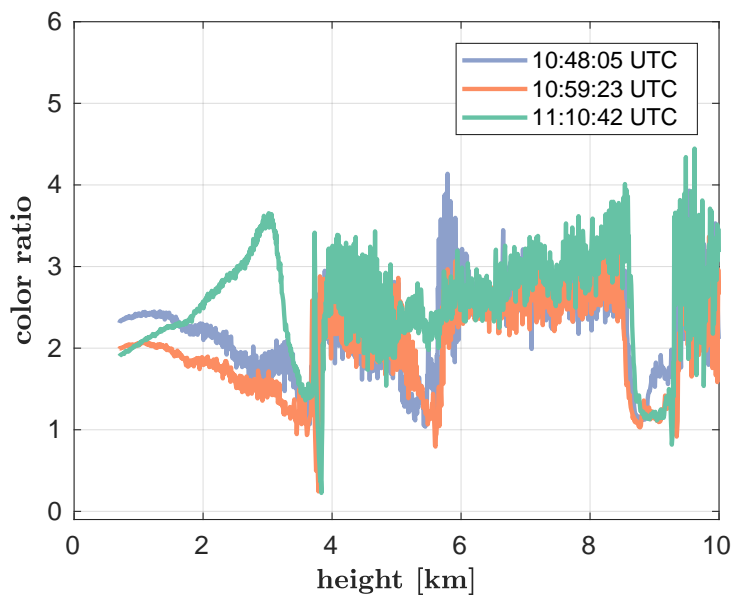
Figure 4.21.: Color ratio profiles from 11:10:42 UTC, 10:59:23 UTC and 10:48:05 UTC from the 31st of July 2021 are displayed. They illustrate the temporal development of the color ratio. Low color ratio is seen at positions of the three clouds, indicating large particles. The color ratio of the intermediate cloud rises for the fifth time step again. This coincides with observed decrease in backscatter.

a second development forms. Measuring errors regarding the humidity profile, or temporal and spatial measurement shifts of lidar and radiosonde are possible. The color ratio decreases as backscatter increases. Moreover, again higher backscatter values at same humidity are parallel to larger particles. Hygroscopic growth is visible for the lower cloud, too.

The hygroscopic behaviour of the intermediate cloud is illustrated in figure 4.23b. The backscatter increases sharply beginning at $72\,\%$ relative humidity over water. The particles grow simultaneously as indicated by the color ratio. Above $80\,\%$ relative humidity, two trends are present. The first one consists of big particles, hence high backscatter, while the second trend shows low backscatter and particle size. This coincides with the profiles of figure 4.18. The backscatter peak is slimmer than the corresponding humidity peak. Therefore, low backscatter values are observed at high humidity, too. Despite this, the first trend of figure 4.23b, where backscatter and particle size increase with humidity, demonstrates hygroscopic growth.

To conclude, multiple cloud layers are present for this day. Two highly variable water clouds are in $3.0 - 3.9\,\text{km}$ and $5.2 - 5.8\,\text{km}$. The lower cloud grows strongly with time, as the intermediate cloud first grows and then begins to vanish. The increase of the lower cloud is that high, that multiple scattering occurs for the last two time steps. In addition, an ice cloud is observed between $8.5\,\text{km}$ and $9.5\,\text{km}$. In comparison to both of the lower clouds, it is stable
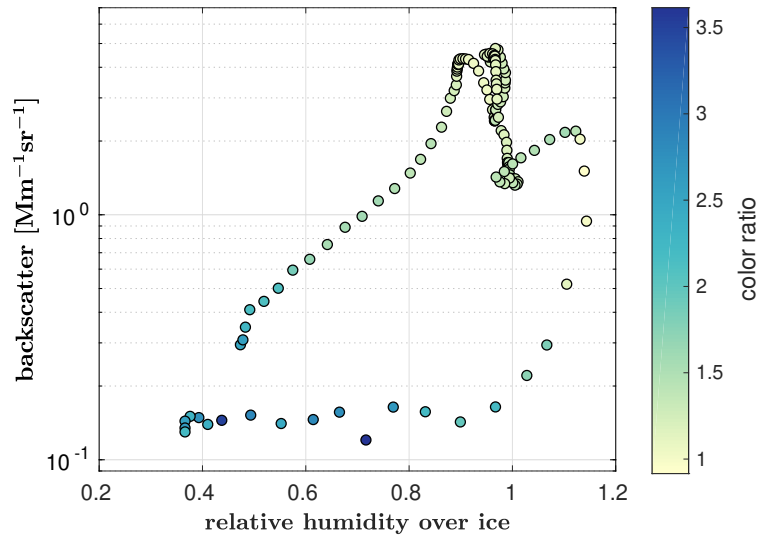
Figure 4.22.: The backscatter of the 31st of July 2021 is plotted against the relative humidity over ice for the interval $8.5 - 9.5\,\mathrm{km}$. This is the position of the ice cloud. The aerosols follow either a hygroscopic development or a non-hygroscopic in this scatter plot. The color map depends on the color ratio. It indicates the occurrence of hygroscopic growth because the color ratio rises with increasing backscatter, parallel to rising humidity.

in time. Since the growth of the two water clouds is very strong, unnatural causes needed to be investigated, i.e. a *feeder-seeder effect* by the upper ice cloud. This effect was ruled out because no ice particles are observed at the lower clouds. Therefore and because of the high variability of the water clouds, temporal and spatial shifts of the lidar and radiosonde measurement are expected to be critical here and lead to a inconsistency of backscatter and humidity profiles. In future studies, a smaller temporal resolution of the lidar data should be used to achieve a better accordance of radiosonde and lidar measurement.
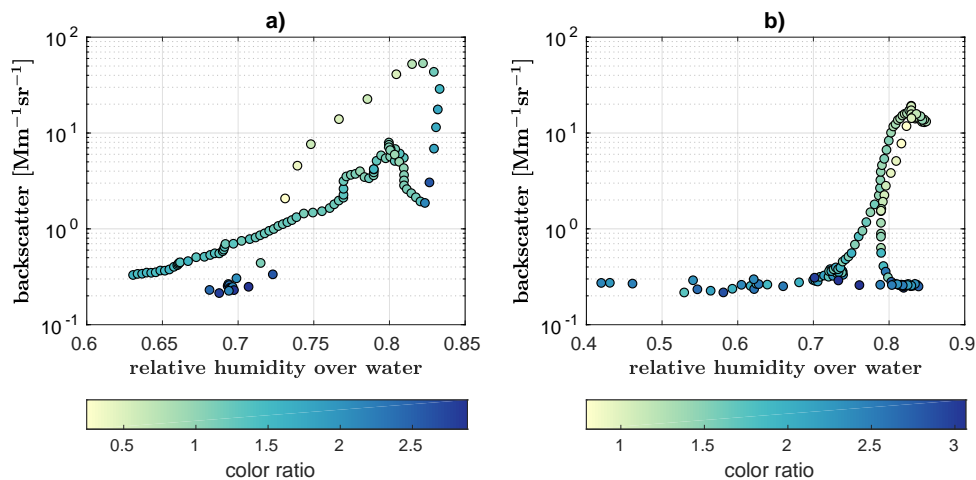
Figure 4.23.: The backscatter of the 31st of July 2021 is plotted against the relative humidity over water for the intervals $3.07 - 3.9\,\mathrm{km}$ (a) and $5.0 - 5.97\,\mathrm{km}$ (b). These are the positions of the humidity gradients of the lower and intermediate clouds. The lower cloud provides a linear correlation of backscatter and humidity. The trend gets chaotic above $77\,\%$ relative humidity. The backscatter of the intermediate cloud rises strongly at certain relative humidity, but is low afterwards. These two fluctuations at high humidity probably stem from shifts between radiosonde and lidar measurement. The color map depends on the color ratio. Hygroscopic growth is indicated for both height intervals.

5. Discussion

Previously shown results of section 4 are compared with other researches. Moreover, evaluations and further interpretations are examined here.

5.1. Seasonal trends in microphysical aerosol properties

The aim of this subsection is to discuss whether the annual cycle of aerosol concentrations in the free Arctic troposphere, proposed by Shibata et al. (2018) and Tunved et al. (2013), coincides with the observed data from 2021. Furthermore, the seasonality of aerosol sorts is to be examined and compared to studies of Tunved et al. (2013) and Quinn et al. (2007) that are summarized in subsection 2.2.

The observed backscatter profile during the haze season in subsection 4.1 differs partially from results of Tunved et al. (2013). After a break in April, the Arctic haze resumes in May and lasts until end of the month. However, the decrease of aerosol concentration in sunlit summer coincides with the decline of backscatter in transition of May and June 2021. In accordance with Tunved et al. (2013), this phenomenon can be classified as disappearance of Arctic haze, coupled with formation of new particles. Formation of particles increases the number concentration of aerosols. Nevertheless these particles are too small for the lidar. Hence, the backscatter decreases, and the color ratio increases, indicating smaller particles. The rise in July probably stems from forest fire aerosols. Due to interannual variability of forest fire events, no accordance with other researches of Arctic aerosol cycles is expected.
Taking a look on the color ratio, one finds a decrease in aerosol size, but of lower gradient than Tunved et al. (2013). However, the whole atmosphere above the lidar was measured and integrated. This leads to a reduced gradient of aerosol development per time. Hence, Tunved et al. (2013) will show clearer, stronger developments of the aerosol.
Overall, one hypothesis regarding the development in 2021 is that the observed progression of Tunved et al. (2013) overlaps with the additional aerosol accumulation of May 2021.

Regarding the fluctuations, a smoother curve is visible in Tunved et al. (2013) than in 2021. They observed the aerosol number distribution and averaged over 10 years. Moreover, they measured at the Zeppelin station, and not in Ny-Ålesund. Therefore, small differences with respect to results of 2021 are expected. The smoother development in Tunved et al. (2013)

makes sense, too.

Quinn et al. (2007) locates the maximum of Arctic haze in March or April. The time of the Arctic haze maximum in 2021 is uncertain. It was found that May 2021 belongs to the haze and might represent the maximum of the haze period. Then again, March 2021 can have even greater extent of Arctic haze.

Shibata et al. (2018) investigated the profile of monthly averaged backscatter, depolarisation and color ratio, as well as time resolved averaged backscatter and depolarisation data, from Arctic aerosol measurements of 2014 to 2017.
Not only did they identify annual cycles that are most pronounced above 2 km, but also they find the aerosol concentration to sink with altitude by order of one magnitude through out the troposphere. In 2021 the backscatter decreases as well with altitude, in particular by up to one magnitude in summer season. Furthermore, the aerosol development of summer 2021 is most pronounced above 2.5 km. This goes with the fact, that the general annual cycle above 2 km is most explicit (Shibata et al., 2018). The overall progression of aerosol backscatter coincides with results of Shibata et al. (2018) above 2 km. However, findings of them also show an interannual variability. Therefore the maximum of mean backscatter can merely be located between May and July. Yet backscatter developments resemble the profiles of 2021, for instance in 2015 from $0.7 - 2$ km and $2 - 4$ km and in 2016 from $2 - 4$ km.
The low values of depolarisation coincide with findings of Shibata et al. (2018) and Müller (2019). However, the development is inverted compared to Shibata et al. (2018). They found lowest values in summer and highest in spring. The positive correlation between the backscatter and the depolarisation is as well the opposite in 2021, hence a negative correlation. The discrepancy might result from fluctuations and uncertainties of the lidar measurement, due to the fact that the depolarisation only takes values of a few percent. Nevertheless, one has to consider the influence of the cloud filter. Shibata et al. (2018) find higher depolarisation in $5 - 8$ km and slightly bigger particles than in 2021. This might result from usage of a stronger cloud mask for 2021 data.

The color ratio shows no clear correlation with results of Shibata et al. (2018). The values reach down to 0 or 1 while the ones of 2021 range from approximately 1 to 3. Moreover, the rise in color ratio to summer is not observed by Shibata et al. (2018). But this increasing color ratio makes sense by consideration of new particle formation in summer.

For comparison with aerosols in Ny-Ålesund of 2019 and 2020, one can consult the researches of Rader (2020) and Dube (2021). Note, that an analysis is just partially possible since their thematic focuse lies on the Arctic haze. Hence, they covered lidar measurements from January to April. The general trend of declining backscatter with height is observed in 2019, 2020 and 2021. Dube (2021) and Rader (2020) hypothesize a correlation with shrinking particle sizes, in combination with lower aerosol concentrations. The Arctic haze phenomenon is more

pronounced in 2020 than in 2019. None of the two researches indicate an extended haze season. In 2019 and 2020 the backscatter of the lowest height interval is the highest in February. The backscatter maximum then shifts towards higher altitudes for later months. In April the backscatter maximum is located between $3 - 5\,\text{km}$ (Rader, 2020). The backscatter values of this height intervals are in good accordance with 2021. However, the height dependent Arctic haze development differs. In April 2021 and May 2021, the maximal backscatter lies for all height intervals below $6.5\,\text{km}$ in May. The highest interval provides no difference between April and May. Therefore, no typical shift of the Arctic haze maximum towards higher altitudes is visible between April and May. But it is to be expected, that the unusually extended haze of 2021 does not follow this pattern, since a return of the haze and not an elongated phasing out till May is hypothesized.

In conclusion, the observed backscatter development in 2021 lies in good accordance with results of Shibata et al. (2018). Compared with Tunved et al. (2013) the maximum of May 2021 cannot be confirmed. In the researches of Shibata et al. (2018) and Graßl and Ritter (2019) an interannual variability is visible. This might as well be the reason for discussed differences between the reviewed studies and 2021.

5.2. Hygroscopicity of the aerosols from April to July 2021

The general hygroscopic behaviour of the Arctic aerosols from April to July 2021 was debated in subsection 4.2. Further discussion to individual hygroscopic events followed in subsection 4.3. Aim of this subsection is to compare the observed behaviour of aerosols in humid areas with other researches as well as with the model of the growth curve (Gassó et al., 2000; Zieger et al., 2010).

The general hygroscopic behaviour of Arctic aerosols in 2021 coincides with results of Müller (2019). She investigated the Arctic aerosols of spring 2018. A general hygroscopic behaviour is observed, i.e. increasing backscatter with humidity. The depolarisation stays constant, which results from mostly spherical particles.

Furthermore, Müller (2019) found the hygroscopic growth to decrease with altitude. Such a height dependent trend is also observed in 2021. At same humidity, the lower troposphere provides higher backscatter values than the upper troposphere in 2021. The aerosol concentration might decrease faster with height than the humidity. However, the different chemical composition and transport ways might as well have significant impact on this trend, like proposed by Dube (2021). Another hypothesis might be that the aerosols of lower heights are bigger than those of upper heights. According to Vu et al. (2021) larger particles grow stronger, due to water uptake, than smaller ones. Since the Arctic haze in terms of backscatter is present mostly below $2.5\,\text{km}$, this hypothesis might hold for spring. In subsection 4.1 the color ratio

was found to be higher in upper height intervals than in lower. Nevertheless this change in particle size is small, especially in summer. Therefore, the first hypothesis, regarding the fast decrease of aerosol concentration, is more likely.

Regarding the case study of the 15 th of May 2021, non-hygroscopic behaviour of the aerosols is observable. Dube (2021) detected this behaviour by parts, too. The backscatter takes both, high and low values, at increased humidity (Dube, 2021). Müller (2019) found a disturbance in depolarisation trends by soil, which is non-hygroscopic. The chemical composition of the aerosols of the 15 th of May might as well be the main cause for this non-hygroscopic trend. Furthermore, the chemical composition of the height intervals might differ, leading to variations in hygroscopic behaviour.
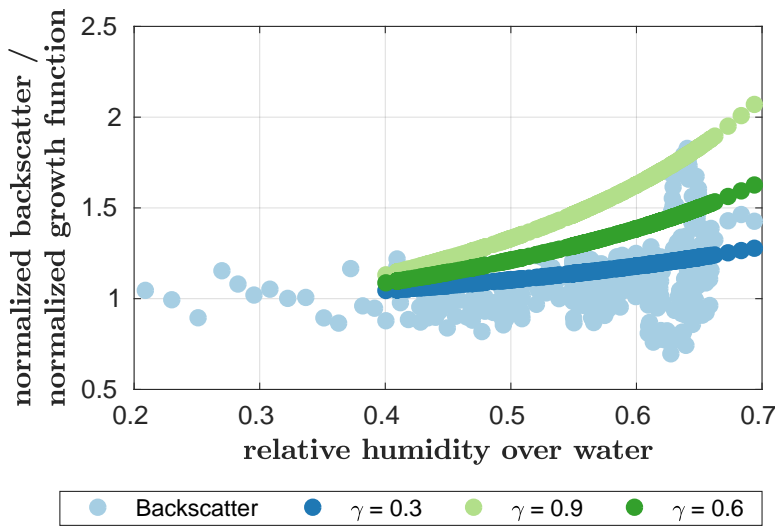

Figure 5.1.: The growth curve of equation 2.2 is fitted to the backscatter of $2.5 - 5.6$ km from the 15th of May 2021. A normalization was made by division with the median backscatter and growth curve values, respectively, of the dry reference interval. The reference stems from in between 20 % and 40 % relative humidity. Therefore, growth curves start at a relative humidity higher than 40 %. Three fit parameters γ for the growth curve are tested, but no growth curve fits the backscatter development. It is still seen, that lower fit parameters γ suit the data better than high ones. Hence, only a small hygroscopic growth is present.

For further investigation of the hygroscopic behaviour, the growth curve in equation 2.2, which is used by Gassó et al. (2000) and Zieger et al. (2010), is fitted on the data of $2.5 - 5.6$ km from 15 th of May in figure 5.1. However, the observed hygroscopic growth does not follow the trend that is proposed by the growth function. No fit parameter γ suits the data, since a strong

rise in backscatter appears already at relatively low humidity. A value $\gamma = 0.3$ almost fits the progress, except for the high rise after 60% relative humidity. High fit parameters can therefore be ruled out. Hence, a lower value than usually detected by Zieger et al. (2010) might suit the data well.

This case study is a good example for the seasonal hygroscopic trend that was investigated in subsection 4.2. The seasonal average fit parameter $\gamma = 0.47$, as well as the obtained parameter $\gamma = 0.3$ from the 15th of May 2021, are lower than expected in terms of studies from Zieger et al. (2010). This makes sense, since Zieger et al. (2010) measured at the Zeppelin station in autumn. No Arctic haze, but more sea salt, which is more hygroscopic, is observed there.

Rader (2020) and Dube (2021) analysed the hygroscopic growth of aerosols in Ny-Ålesund in spring 2019 respectively 2020. Rader (2020) fitted the growth curve on two different days to her data of 2019. Parameters γ often take similar magnitudes as in 2021. Still, higher fit parameters are found by both as well. Since the 15th of May 2021 only displayed a subtle growth behaviour, this difference is understandable.

The growth function of equation 2.2 does not suit the growth of aerosols with respect to humidity over ice, hence the development of ice clouds. It is defined with the humidity over water. Therefore, the growth curve cannot be applied to the ice cloud of the 31 th of July.

6. Conclusion and future work

This section aims to provide a summary of important findings. Afterwards, possible future research on this topic is introduced. In particular, a method to evaluate whether aerosols' size or chemical composition is dominating the scatter plots of backscatter and relative humidity in subsection 4.2 is introduced. Results of this demonstrate a possible focus topic of future hygroscopicity studies.

6.1. Conclusion

In the following a summary of important findings is given.

The investigation of the seasonal change in physical aerosol properties shows an extended haze season till May. A return of the Arctic haze is hypothesized, rather than an elongated time of phasing out. By daily median between $0.7\,\mathrm{km}$ and $10\,\mathrm{km}$, the maximum in May reaches up to $0.2\,\mathrm{Mm}^{-1}\mathrm{sr}^{-1}$. Graßl and Ritter (2019) detected an interannual variability of the Arctic haze, which might coincide with this event. In general, the Arctic haze in terms of backscatter is the strongest in lower altitudes. Nevertheless, the transition of Arctic haze to summer season is most pronounced between $2.5\,\mathrm{km}$ and $6.5\,\mathrm{km}$.

Furthermore, no clear hygroscopic trend is visible, due to the amount of different hygroscopic events. But overall, the median backscatter from April to July 2021 rises with humidity. A fit parameter $\gamma = 0.47$ for the growth curve is found to describe this average hygroscopic growth well. It is equivalent to a seasonal average by assuming that disruptive effects cancel out, due to the large quantity of cases and heights. The seasonal fit parameter is lower than expected, in terms of studies from Zieger et al. (2010). The 15th of May 2021 serves as good example for this weaker hygroscopic behaviour, since a fit parameter $\gamma = 0.3$ was found at this day.

Height and time dependent biases of the hygroscopic growth are detected, too. Lower altitudes show both, higher backscatter and higher relative humditiy. In particular, investigation of the distribution of humidity and backscatter within height show that the aerosol concentration might sink more rapid than the humidity with height. The seasonal research showed that May often provides enhanced backscatter in humid regions.

In addition, two hygroscopic events are examined further. They function as example for disturbances in the hygroscopic behaviour of the general Arctic aerosol. The aerosols of the 15 th of

May 2021 exhibit partially no hygroscopic growth. Natural fluctuations can cause the effect of hygroscopic behaviour. Only by consideration of strong humidity gradients, which adjoin the height interval, a distinction between fluctuation and hygroscopic growth is possible.

The second case study happens on the 31st of July 2021. It includes the occurrence of a rare ice cloud. Moreover, multiple cloud layers are present. Two water clouds underneath the ice cloud demonstrate high temporal fluctuations. A *feeder-seeder effect* by the upper ice cloud was ruled out. Due to the high variability it is expected that the temporal and spatial difference of lidar and radiosonde is critical. Conditions change rapidly, leading to an inconsistency of backscatter and humidity profiles.

6.2. Future work

Some future concepts for continuation and application of the thesis' investigations are stated here.

Poguntke and Ritter (2023) found a continuous disturbance in the lidar signal. A frequency of $5\,\text{MHz}$ impacts the measurements. It might result from old recorders. Dube (2021) already saw this frequency in his data. By means of fourier analysis, this frequency can be filtered out. Thus, a more precise investigation of the lidar signal might be achieved. However, the signal has no big impact on the results of this thesis. Due to frequent usage of the median, the periodic disturbance cancels itself out. Moreover, no strong occurence of oscillations in profiles of the case studies is seen. So invesitgated trends of microphysical aerosol properties stay unchanged, due to the periodic signal.

The second case study in subsection 4.3.2 can also be investigated further. It was observed, that the temporal and spatial shift of the lidar and radiosonde measurement is critical, due to the high variability of the lower two clouds. For a more precise analysis of the cloud formation, the temporal resolution of the lidar needs to be reduced to its minimum of approximately $1.5 - 2.0$ minutes.

According to Stock et al. (2014), the exact origin of Arctic aerosols is still unknown. Due to interannual variability (Graßl and Ritter, 2019), consideration of special occasions is necessary for further understanding of the transport patterns. Implementation of the observed reduction of the Arctic haze, April 2021, might lead to new evidence.

In general, more case studies are needed to improve models of the Arctic aerosol. For instance models of hygroscopic growth or transport patterns can be deepened by implementation of more, frequently occurring trends like non-hygroscopic aerosols, ice clouds and seasonality modulations in microphysical aerosol properties.

Results of this thesis can be used for improving models of the *average Arctic aerosol*. In

particular, figure 4.10 supports the description of the hygroscopic growth. The fitted growth curve in figure 4.11 provides an average growth curve fit parameter γ of the Arctic aerosol. This might be used for a simplified consideration of hygroscopic growth.

This simplified consideration can be made more exact in future studies. Aim of this future study is to investigate whether size or chemical composition of the aerosols is the dominating factor in hygroscopic growth. According to studies of Vu et al. (2021), larger particles often grow stronger than smaller ones. Simultaneously, chemical composition of the aerosols determines the hygroscopic growth, too, as stated by Vu et al. (2015) and Swietlicki et al. (2008). Via suitable subdivision of the data set, one might reduce the scatter of figure 4.10, and obtain more precise average fit parameter γ. The approach is a separation in four subsets: small and big color ratio values, as indication of size, and small and big lidar ratios, as indication of chemical composition. Scatter is hopefully reduced. The hygroscopic growth curves are then determined for all four data sets. Finally, it is evaluated by means of the results, if size or chemical composition is the dominating factor in hygroscopic growth. A schematical illustration of the outlined procedure is gathered in figure 6.1.
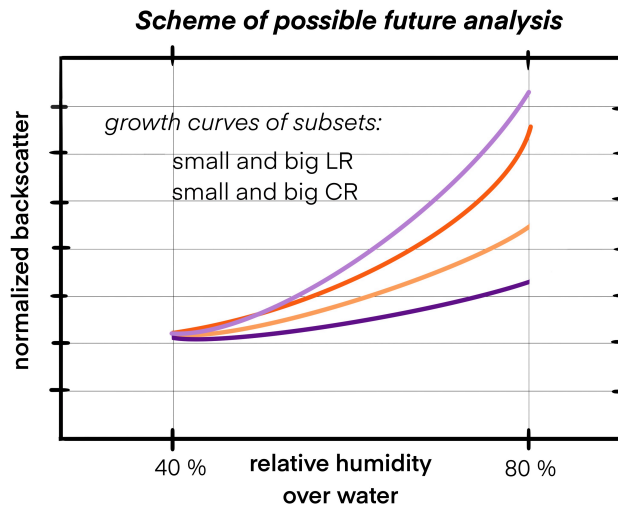

Figure 6.1.: A schematical overview of a possible future study is illustrated. Aim of this study is to reduce the scatter of figure 4.10 and obtain a more precise average fit parameter γ. It is assumed to determine, whether size or chemical composition is the dominating factor of hygroscopic growth. Therefore, one divides the data set of figure 4.10 into four subsets: small and big color ratio, and small and big lidar ratio. Color ratio provides information about the size of aerosols, and lidar ratio about their chemical composition. The growth curve is then identified for all four subsets.

Acknowledgement

Bibliography

Albert Ansmann, Ulla Wandinger, Maren Riebesell, Claus Weitkamp, and Walfried Michaelis. Independent measurement of extinction and backscatter profiles in cirrus clouds by using a combined raman elastic-backscatter lidar. *Appl. Opt.*, 31(33):7113–7131, Nov 1992. doi: 10.1364/AO.31.007113. URL https://opg.optica.org/ao/abstract.cfm?URI=ao-31-33-7113.

Olivier Boucher. *Atmospheric Aerosols: Properties and Climate Impacts*. Springer, Dordrecht, 1 edition, 2015. ISBN 978-94-017-9648-4.

Anthony Bucholtz. Rayleigh-scattering calculations for the terrestrial atmosphere. *Appl. Opt.*, 34(15):2765–2773, May 1995. doi: 10.1364/AO.34.002765. URL https://opg.optica.org/ao/abstract.cfm?URI=ao-34-15-2765.

Susannah M. Burrows, Christina S. McCluskey, Gavin Cornwell, Isabelle Steinke, Kai Zhang, Bin Zhao, Maria Zawadowicz, Aishwarya Raman, Gourihar Kulkarni, Swarup China, Alla Zelenyuk, and Paul J. DeMott. Ice-nucleating particles that impact clouds and climate: Observational and modeling research needs. *Reviews of Geophysics*, 60 (2):e2021RG000745, 2022. doi: https://doi.org/10.1029/2021RG000745. URL https://agupubs.onlinelibrary.wiley.com/doi/abs/10.1029/2021RG000745. e2021RG000745 2021RG000745.

Judith A. Curry, Julie L. Schramm, William B. Rossow, and David Randall. Overview of arctic cloud and radiation characteristics. *Journal of Climate*, 9:1731–1764, Aug 1996. doi: https://doi.org/10.1175/1520-0442(1996)009<1731: OOACAR>2.0.CO;2. URL https://journals.ametsoc.org/view/journals/clim/9/8/1520-0442_1996_009_1731_ooacar_2_0_co_2.xml?tab_body=abstract-display.

Wolfgang Demtröder. *Experimentalphysik 3 : Atome, Moleküle und Festkörper*. Heidelberg : Springer Spektrum, Berlin, 5 edition, 2016. ISBN 978-3-662-49094-5. doi: https://doi.org/10.1007/978-3-662-49094-5.

Jonas Dube. Physikalische Eigenschaften troposphärischen Aerosols abgeleitet aus Lidar-Daten aus der europäischen Arktis im Frühjahr 2020s, Jul 2021.

Thomas Foken. *Springer Handbook of Atmospheric Measurements*. Springer Cham, 1 edition, Nov 2021. ISBN 978-3-030-52171-4. doi: https://doi.org/10.1007/978-3-030-52171-4.

S. Gassó, D. A. Hegg, D. S. Covert, D. Collins, K. J. Noone, E. Öström, B. Schmid, P. B. Russell, J. M. Livingston, P. A. Durkee, and H. Jonsson. Influence of humidity on the aerosol scattering coefficient and its effect on the upwelling radiance during ace-2. *Tellus B: Chemical and Physical Meteorology*, 52(2):546–567, 2000. doi: 10.3402/tellusb.v52i2.16657. URL `https://doi.org/10.3402/tellusb.v52i2.16657`.

Sandra Graßl and Christoph Ritter. Properties of Arctic Aerosol Based on Sun Photometer Long-Term Measurements in Ny-Ålesund, Svalbard. *Remote Sensing*, 11(11), 2019. ISSN 2072-4292. doi: 10.3390/rs11111362. URL `https://www.mdpi.com/2072-4292/11/11/1362`.

Dennis L. Hartmann, E. Maureen, Ockert-Bell, and Marc L. Michelsen. The Effect of Cloud Type on Earth's Energy Balance: Global Analysis. *Journal of Climate*, 5(11):1281–1304, Nov 1992. doi: 10.1175/1520-0442(1992)005<1281:TEOCTO>2.0.CO;2. URL `https://doi.org/10.1175/1520-0442(1992)005<1281:TEOCTO>2.0.CO;2`.

James Haywood and Olivier Boucher. Estimates of the direct and indirect radiative forcing due to tropospheric aerosols: A review. *Reviews of Geophysics*, 38(4):513–543, 2000. doi: https://doi.org/10.1029/1999RG000078. URL `https://agupubs.onlinelibrary.wiley.com/doi/abs/10.1029/1999RG000078`.

Anne Hoffmann. *Comparative aerosol studies based on multi-wavelength Raman LIDAR at Ny-Ålesund, Spitsbergen*. doctoralthesis, Universität Potsdam, 2011.

IPCC. *Climate Change 2021: The Physical Science Basis. Contribution of Working Group I to the Sixth Assessment Report of the Intergovernmental Panel on Climate Change*, page 33144. Cambridge University Press, Cambridge, United Kingdom and New York, NY, USA, 2021. doi: 10.1017/9781009157896.002.

James D. Klett. Stable analytical inversion solution for processing lidar returns. *Appl. Opt.*, 20(2):211–220, Jan 1981. doi: 10.1364/AO.20.000211. URL `https://opg.optica.org/ao/abstract.cfm?URI=ao-20-2-211`.

Jacqueline Lenoble, Lorraine Remer, and Didier Tanre. *Aerosol Remote Sensing*. Springer Berlin, Heidelberg, 1 edition, 2013. ISBN 978-3-642-17725-5. doi: https://doi.org/10.1007/978-3-642-17725-5.

Jing Li, Barbara E. Carlson, Yuk L. Yung, Daren Lv, James Hansen, Joyce E. Penner, Hong Liao, V. Ramaswamy, Ralph A. Kahn, Peng Zhang, Oleg Dubovik, Aijun Ding, Andrew A. Lacis, Lu Zhang, and Yueming Dong. Scattering and absorbing aerosols in the climate

system. *Nature Reviews Earth & Environment*, 3(6):363–379, Jun 2022. ISSN 2662-138X. doi: 10.1038/s43017-022-00296-7. URL `https://doi.org/10.1038/s43017-022-00296-7`.

U. Lohmann and J. Feichter. Global indirect aerosol effects: a review. *Atmospheric Chemistry and Physics*, 5(3):715–737, 2005. doi: 10.5194/acp-5-715-2005. URL `https://acp.copernicus.org/articles/5/715/2005/`.

Gustav Mie. Beiträge zur Optik trüber Medien, speziell kolloidaler Metallösungen. *Annalen der Physik*, 330(3):377–445, 1908. doi: https://doi.org/10.1002/andp.19083300302. URL `https://onlinelibrary.wiley.com/doi/abs/10.1002/andp.19083300302`.

Vaios Moschos, Katja Dzepina, Deepika Bhattu, Houssni Lamkaddam, Roberto Casotto, Kaspar R. Daellenbach, Francesco Canonaco, Pragati Rai, Wenche Aas, Silvia Becagli, Giulia Calzolai, Konstantinos Eleftheriadis, Claire E. Moffett, Jürgen Schnelle-Kreis, Mirko Severi, Sangeeta Sharma, Henrik Skov, Mika Vestenius, Wendy Zhang, Hannele Hakola, Heidi Hellén, Lin Huang, Jean-Luc Jaffrezo, Andreas Massling, Jakob K. Nøjgaard, Tuukka Petäjä, Olga Popovicheva, Rebecca J. Sheesley, Rita Traversi, Karl Espen Yttri, Julia Schmale, André S. H. Prévôt, Urs Baltensperger, and Imad El Haddad. Equal abundance of summertime natural and wintertime anthropogenic Arctic organic aerosols. *Nature Geoscience*, 15(3):196–202, Mar 2022. ISSN 1752-0908. doi: 10.1038/s41561-021-00891-1. URL `https://doi.org/10.1038/s41561-021-00891-1`.

Kim Janka Müller. Characterisation of arctic aerosols on the basis of lidar- and radiosonde-data. Master's thesis, Carl von Ossietzky Universität, Oldenburg, Feb 2019.

Konstantina Nakoudi, Christoph Ritter, Christine Böckmann, Daniel Kunkel, Oliver Eppers, Vladimir Rozanov, Linlu Mei, Vasileios Pefanis, Evelyn Jäkel, Andreas Herber, Marion Maturilli, and Roland Neuber. Does the intra-arctic modification of long-range transported aerosol affect the local radiative budget? (a case study). *Remote Sensing*, 12(13), 2020. ISSN 2072-4292. doi: 10.3390/rs12132112. URL `https://www.mdpi.com/2072-4292/12/13/2112`.

Konstantina Nakoudi, Iwona S. Stachlewska, and Christoph Ritter. An extended lidar-based cirrus cloud retrieval scheme: first application over an arctic site. *Opt. Express*, 29(6):8553–8580, Mar 2021. doi: 10.1364/OE.414770. URL `https://opg.optica.org/oe/abstract.cfm?URI=oe-29-6-8553`.

NASA earth observatory. Glossary - Radiosonde. `https://earthobservatory.nasa.gov/glossary/radiosonde`. Accessed: 2023-06-19.

NASA earth observatory. Clouds & Radiation Fact Sheet, Mar 1999. URL `https://earthobservatory.nasa.gov/features/Clouds`. Last accessed: 2023-03-14.

Joyce E. Penner, Sophia Y. Zhang, and Catherine C. Chuang. Soot and smoke aerosol may not warm climate. *Journal of Geophysical Research: Atmospheres*, 108(D21), 2003. doi: https://doi.org/10.1029/2003JD003409. URL `https://agupubs.onlinelibrary.wiley.com/doi/abs/10.1029/2003JD003409`.

T. Poguntke and C. Ritter. Influence of Electromagnetic Interference on the evaluation of Lidar-derived Aerosol properties from Ny-Ålesund, Svalbard. 2023.

P. K. Quinn, G. Shaw, E. Andrews, E. G. Dutton, T. Ruoho-Airola, and S. L. Gong. Arctic haze: current trends and knowledge gaps. *Tellus B: Chemical and Physical Meteorology*, 59 (1):99–114, 2007. doi: 10.1111/j.1600-0889.2006.00236.x. URL `https://doi.org/10.1111/j.1600-0889.2006.00236.x`.

Fieke Rader. Characteristics and physical properties of arctic aerosols. Master's thesis, Technische Universität Berlin, Oct 2020.

A. Rinke, K. Dethloff, and M. Fortmann. Regional climate effects of arctic haze. *Geophysical Research Letters*, 31(16), 2004. doi: https://doi.org/10.1029/2004GL020318. URL `https://agupubs.onlinelibrary.wiley.com/doi/abs/10.1029/2004GL020318`.

Walter Roedel and Thomas Wagner. *Physik unserer Umwelt: Die Atmosphäre*. Springer Spektrum Berlin, Heidelberg, 5 edition, 2018. ISBN 978-3-662-54258-3. doi: https://doi.org/10.1007/978-3-662-54258-3.

Daniel Rosenfeld, Meinrat O. Andreae, Ari Asmi, Mian Chin, Gerrit de Leeuw, David P. Donovan, Ralph Kahn, Stefan Kinne, Niku Kivekäs, Markku Kulmala, William Lau, K. Sebastian Schmidt, Tanja Suni, Thomas Wagner, Martin Wild, and Johannes Quaas. Global observations of aerosol-cloud-precipitation-climate interactions. *Reviews of Geophysics*, 52(4):750–808, 2014. doi: https://doi.org/10.1002/2013RG000441. URL `https://agupubs.onlinelibrary.wiley.com/doi/abs/10.1002/2013RG000441`.

Julia Schmale, Paul Zieger, and Annica M. L. Ekman. Aerosols in current and future Arctic climate. *Nature Climate Change*, 11(2):95–105, Feb 2021. ISSN 1758-6798. doi: 10.1038/s41558-020-00969-5. URL `https://doi.org/10.1038/s41558-020-00969-5`.

T. Shibata, K. Shiraishi, M. Shiobara, S. Iwasaki, and T. Takano. Seasonal Variations in High Arctic Free Tropospheric Aerosols Over Ny-Ålesund, Svalbard, Observed by Ground-Based Lidar. *Journal of Geophysical Research: Atmospheres*, 123(21):12,353–12,367, 2018. doi: https://doi.org/10.1029/2018JD028973. URL `https://agupubs.onlinelibrary.wiley.com/doi/abs/10.1029/2018JD028973`.

Maria Stock, Christoph Ritter, Veijo Aaltonen, Wenche Aas, Dörthe Handorff, Andreas Herber, Renate Treffeisen, and Klaus Dethloff. Where does the optically detectable aerosol in the

European Arctic come from? *Tellus B: Chemical and Physical Meteorology*, 66(1):21450, 2014. doi: 10.3402/tellusb.v66.21450. URL `https://doi.org/10.3402/tellusb.v66.21450`.

A. Stohl. Characteristics of atmospheric transport into the arctic troposphere. *Journal of Geophysical Research: Atmospheres*, 111(D11), 2006. doi: https://doi.org/10.1029/2005JD006888. URL `https://agupubs.onlinelibrary.wiley.com/doi/abs/10.1029/2005JD006888`.

Johan Ström, Ann Christine Engvall, Frank Delbart, Radovan Krejci, and Renate Treffeisen. On small particles in the arctic summer boundary layer: observations at two different heights near ny-Ålesund, svalbard. *Tellus B: Chemical and Physical Meteorology*, 61(2):473–482, 2009. doi: 10.1111/j.1600-0889.2009.00412.x. URL `https://www.tandfonline.com/doi/abs/10.1111/j.1600-0889.2009.00412.x`.

E. Swietlicki, H. C. Hansson, K. Hämeri, B. Svenningsson, A. Massling, G. Mcfiggans, P. H. Mcmurry, T. Petäjä, P. Tunved, M. Gysel, D. Topping, E. Weingartner, U. Baltensperger, J. Rissler, A. Wiedensohler, and M. Kulmala. Hygroscopic properties of submicrometer atmospheric aerosol particles measured with h-tdma instruments in various environments—a review. *Tellus B: Chemical and Physical Meteorology*, 60(3):432–469, 2008. doi: 10.1111/j.1600-0889.2008.00350.x. URL `https://doi.org/10.1111/j.1600-0889.2008.00350.x`.

Ignatius N. Tang. Chemical and size effects of hygroscopic aerosols on light scattering coefficients. *Journal of Geophysical Research: Atmospheres*, 101(D14):19245–19250, 1996. doi: https://doi.org/10.1029/96JD03003. URL `https://agupubs.onlinelibrary.wiley.com/doi/abs/10.1029/96JD03003`.

P. Tunved, J. Ström, and R. Krejci. Arctic aerosol life cycle: linking aerosol size distributions observed between 2000 and 2010 with air mass transport and precipitation at Zeppelin station, Ny-Ålesund, Svalbard. *Atmospheric Chemistry and Physics*, 13(7):3643–3660, 2013. doi: 10.5194/acp-13-3643-2013. URL `https://acp.copernicus.org/articles/13/3643/2013/`.

S. Twomey. The influence of pollution on the shortwave albedo of clouds. *Journal of Atmospheric Sciences*, 34(7):1149 – 1152, 1977. doi: https://doi.org/10.1175/1520-0469(1977)034<1149:TIOPOT>2.0.CO;2. URL `https://journals.ametsoc.org/view/journals/atsc/34/7/1520-0469_1977_034_1149_tiopot_2_0_co_2.xml`.

Tuan V. Vu, Juana Maria Delgado-Saborit, and Roy M. Harrison. A review of hygroscopic growth factors of submicron aerosols from different sources and its implication for calculation of lung deposition efficiency of ambient aerosols. *Air Quality, Atmosphere & Health*, 8(5):429–440, Oct 2015. ISSN 1873-9326. doi: 10.1007/s11869-015-0365-0. URL `https://doi.org/10.1007/s11869-015-0365-0`.

Tuan V. Vu, Zongbo Shi, and Roy M. Harrison. Estimation of hygroscopic growth properties of source-related sub-micrometre particle types in a mixed urban aerosol. *npj Climate and Atmospheric Science*, 4(1):21, Mar 2021. ISSN 2397-3722. doi: 10.1038/s41612-021-00175-w. URL `https://doi.org/10.1038/s41612-021-00175-w`.

C. Warneke, K. D. Froyd, J. Brioude, R. Bahreini, C. A. Brock, J. Cozic, J. A. de Gouw, D. W. Fahey, R. Ferrare, J. S. Holloway, A. M. Middlebrook, L. Miller, S. Montzka, J. P. Schwarz, H. Sodemann, J. R. Spackman, and A. Stohl. An important contribution to springtime arctic aerosol from biomass burning in russia. *Geophysical Research Letters*, 37(1), 2010. doi: https://doi.org/10.1029/2009GL041816. URL `https://agupubs.onlinelibrary.wiley.com/doi/abs/10.1029/2009GL041816`.

Claus Weitkamp. *Range-Resolved Optical Remote Sensing of the Atmosphere*. Springer New York, NY, 1 edition, 2006. ISBN 978-0-387-25101-1. doi: https://doi.org/10.1007/b106786.

P. Winiger, T. E. Barrett, R. J. Sheesley, L. Huang, S. Sharma, L. A. Barrie, K. E. Yttri, N. Evangeliou, S. Eckhardt, A. Stohl, Z. Klimont, C. Heyes, I. P. Semiletov, O. V. Dudarev, A. Charkin, N. Shakhova, H. Holmstrand, A. Andersson, and Ö. Gustafsson. Source apportionment of circum-arctic atmospheric black carbon from isotopes and modeling. *Science Advances*, 5(2):eaau8052, 2019. doi: 10.1126/sciadv.aau8052. URL `https://www.science.org/doi/abs/10.1126/sciadv.aau8052`.

P. Zieger, R. Fierz-Schmidhauser, M. Gysel, J. Ström, S. Henne, K. E. Yttri, U. Baltensperger, and E. Weingartner. Effects of relative humidity on aerosol light scattering in the arctic. *Atmospheric Chemistry and Physics*, 10(8):3875–3890, 2010. doi: 10.5194/acp-10-3875-2010. URL `https://acp.copernicus.org/articles/10/3875/2010/`.

P. Zieger, R. Fierz-Schmidhauser, E. Weingartner, and U. Baltensperger. Effects of relative humidity on aerosol light scattering: results from different european sites. *Atmospheric Chemistry and Physics*, 13(21):10609–10631, 2013. doi: 10.5194/acp-13-10609-2013. URL `https://acp.copernicus.org/articles/13/10609/2013/`.

Tymon Zielinski, Ezio Bolzacchini, Marco Cataldi, Luca Ferrero, Sandra Graßl, Georg Hansen, David Mateos, Mauro Mazzola, Roland Neuber, Paulina Pakszys, Michal Posyniak, Christoph Ritter, Mirko Severi, Piotr Sobolewski, Rita Traversi, and Christian Velasco-Merino. Study of chemical and optical properties of biomass burning aerosols during long-range transport events toward the arctic in summer 2017. *Atmosphere*, 11(1), 2020. ISSN 2073-4433. doi: 10.3390/atmos11010084. URL `https://www.mdpi.com/2073-4433/11/1/84`.

Anders Ångström. The parameters of atmospheric turbidity. *Tellus*, 16(1):64–75, 1964. doi: 10.3402/tellusa.v16i1.8885. URL `https://doi.org/10.3402/tellusa.v16i1.8885`.

A. Percentiles of backscatter

0.7 - 10 km				
percentile	April [Mm^{-1}sr^{-1}]	May [Mm^{-1}sr^{-1}]	June [Mm^{-1}sr^{-1}]	July [Mm^{-1}sr^{-1}]
0.25	0.0963	0.0971	0.0445	0.1415
0.5	0.1188	0.1367	0.0613	0.1766
0.75	0.1534	0.2515	0.1276	0.2315
0.7 - 2.5 km				
percentile	April [Mm^{-1}sr^{-1}]	May [Mm^{-1}sr^{-1}]	June [Mm^{-1}sr^{-1}]	July [Mm^{-1}sr^{-1}]
0.25	0.2288	0.4160	0.1679	0.3061
0.5	0.2910	0.5146	0.2187	0.3566
0.75	0.4481	0.5734	0.3683	0.4909
6.5 - 10 km				
percentile	April [Mm^{-1}sr^{-1}]	May [Mm^{-1}sr^{-1}]	June [Mm^{-1}sr^{-1}]	July [Mm^{-1}sr^{-1}]
0.25	0.0750	0.0695	0.04720	0.1229
0.50	0.0937	0.0928	0.05744	0.1363
0.75	0.1104	0.1278	0.07244	0.1649

Table A.1.: The 25th, 50th and 75th percentile of the backscatter are gathered by month for three different height intervals. The backscatter development follows the results of subsection 4.1, meaning maximum backscatter values in May and a decline towards June. Together with table 4.1, which includes the corresponding percentiles for the humidity, it is visible that the aerosols from May differ from the ones of the summer season, i.e. July. The hypothesis of Arctic haze pollution in May is stressed.

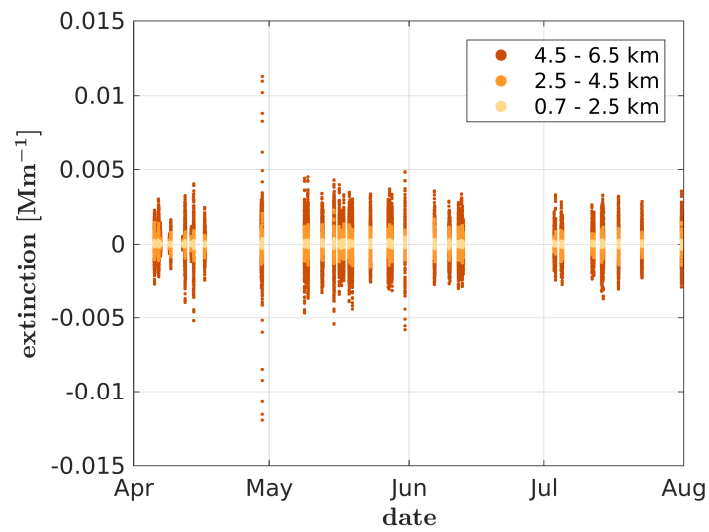# B. Comparison of noise in extinction for different height intervals

Figure B.1.: The extinction values of each measurement day from April 2021 to July 2021 are displayed for the three different height intervals $0.7 - 2.5\,\mathrm{km}$, $2.5 - 4.5\,\mathrm{km}$ and $4.5 - 6.5\,\mathrm{km}$. The range of values is significantly higher and also takes strongly negative values for the upper two intervals. The fluctuation is too high above $2.5\,\mathrm{km}$. Therefore these extinction values are not evaluated further.

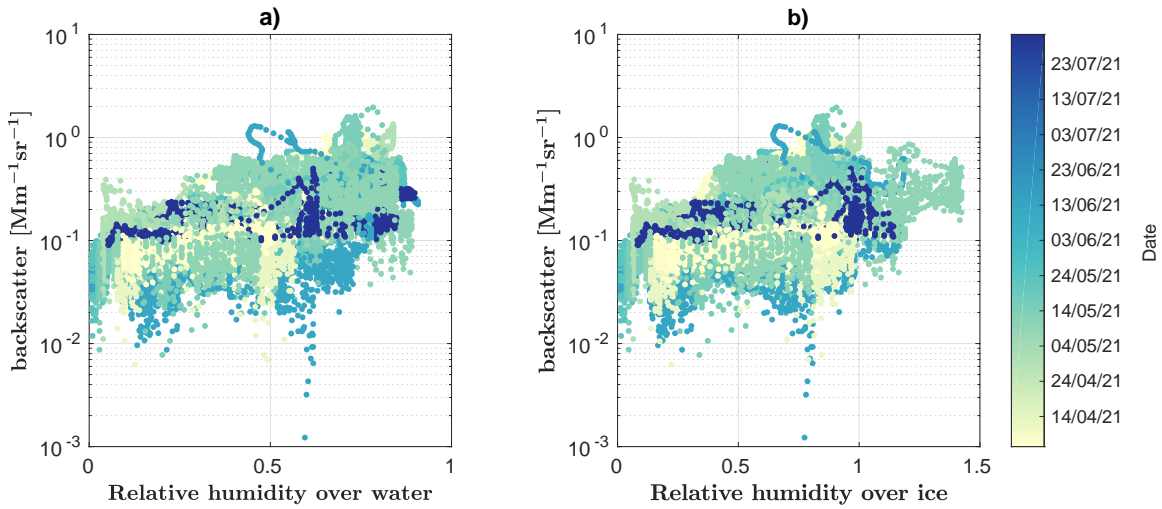# C. Seasonal trends of hygroscopic growth

Figure C.1.: The scatter plot illustrates all time steps from April 2021 to July 2021, that pass the cloud filter. The backscatter is plotted against the relative humidity over water (a) and over ice (b), respectively. The color map is time depend. Measurements from $0.7 - 10\,\mathrm{km}$ are shown. It is important to consider the order of plotting the data points. All time steps of one height step were plotted before going to the next height. So data points of lower heights might be covered. April seems to be the most dry, or other data points are covered. In May it is likely that high backscatter values occur parallel to enhanced humidity.
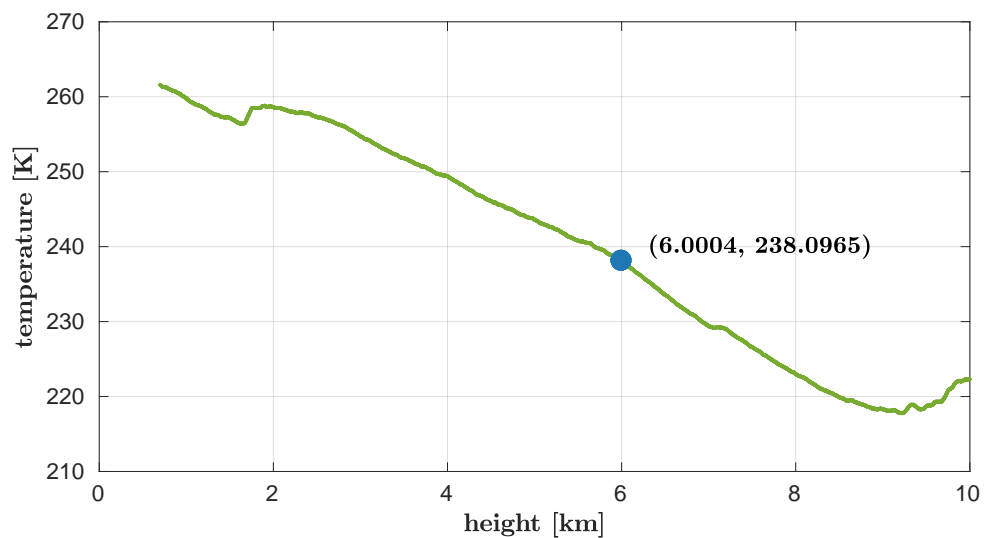
D. Temperature profile of the 15th of May 2021

Figure D.1.: The temperature profile of the radiosonde measurement from the 15th of May 2021 at 10:46:10 UTC is displayed. Above approximately $6\,\mathrm{km}$ the temperature is lower than $-35°\mathrm{C}$. It is assumed that below $-35\,°\mathrm{C}$ only the relative humidity over ice is relevant. Due to the rarity of INP, above $-35\,°\mathrm{C}$ is then only the relative humidity over water to be observed.

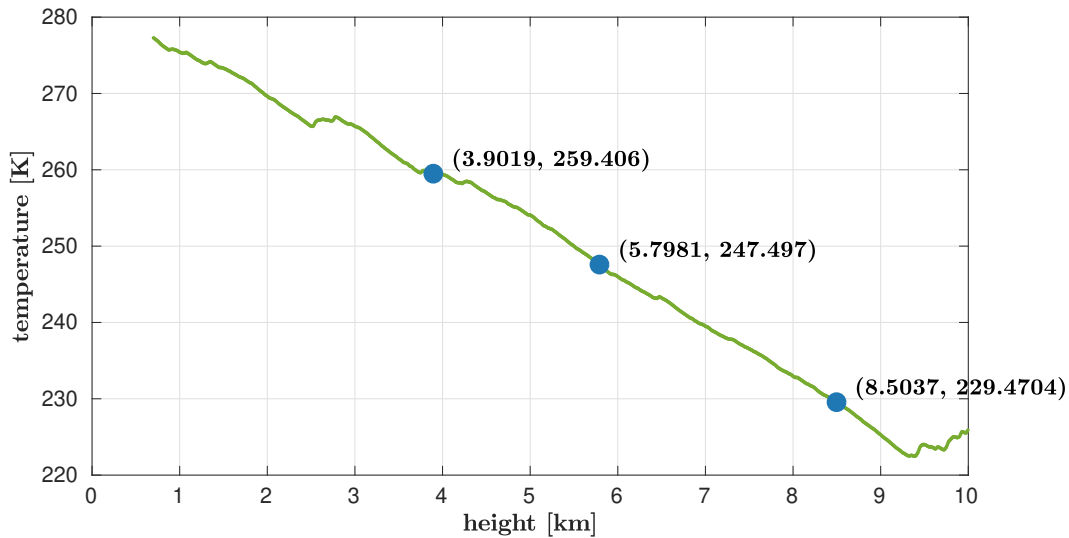# E. Temperature profile of the 31st of July 2021

Figure E.1.: The temperature profile of the radiosonde measurement from the 31st of July 2021 at 10:49:03 UTC is displayed. At position of the lower cloud, meaning from $3.0 - 3.9\,\mathrm{km}$, the temperature amounts to $259\,\mathrm{K} - 266\,\mathrm{K}$. The intermediate cloud has temperatures of above $247\,\mathrm{K}$. No ice cloud is expected for these temperatures. The temperature at position of the upper cloud is low enough. Therefore, the hypothesis of an ice cloud is stressed.